

Texture Memory in Hexagonal Metals and Its Mechanism

Toshiro Tomida ^{1,*}, Sven C. Vogel ² , Yusuke Onuki ¹  and Shigeo Sato ^{1,3} 

¹ Frontier Research Center for Applied Atomic Sciences, Ibaraki University, Naka 319-1106, Ibaraki, Japan; yusuke.onuki.0@vc.ibaraki.ac.jp (Y.O.); shigeo.sato.ar@vc.ibaraki.ac.jp (S.S.)

² Los Alamos Neutron Science Center, Los Alamos National Laboratory, Los Alamos, NM 87545, USA; sven@lanl.gov

³ Graduate School of Science and Engineering, Ibaraki University, Hitachi 316-8511, Ibaraki, Japan

* Correspondence: toshiro.tomida.tomida_tsr@vc.ibaraki.ac.jp

Abstract: Texture memory is a phenomenon in which retention of initial textures occurs after a complete cycle of forward and backward transformations, and it occurs in various phase-transforming materials including cubic and hexagonal metals such as steels and Ti and Zr alloys. Texture memory is known to be caused by the phenomena called variant selection, in which some of the allowed child orientations in an orientation relationship between the parent and child phases are preferentially selected. Without such variant selection, the phase transformations would randomize preferred orientations. In this article, the methods of prediction of texture memory and mechanisms of variant selections in hexagonal metals are explored. The prediction method using harmonic expansion of orientation distribution functions with the variant selection in which the Burgers orientation relationship, $\{110\}_{\beta} // \{0001\}_{\alpha\text{-hex}} <1\bar{1}1>_{\beta} // \langle 2\bar{1}\bar{1}0 \rangle_{\alpha\text{-hex}}$, is held with two or more adjacent parent grains at the same time, called “double Burgers orientation relation (DBOR)”, is introduced. This method is shown to be a powerful tool by which to analyze texture memory and ultimately provide predictive capabilities for texture changes during phase transformations. Variation in nucleation and growth rates on special boundaries and an extensive growth of selected variants are also described. Analysis of textures of commercially pure Ti observed in situ by pulsed neutron diffraction reveals that the texture memory in CP-Ti is indeed quite well predicted by consideration of the mechanism of DBOR. The analysis also suggests that the nucleation and growth rates on the special boundary of 90° rotation about $\langle 2\bar{1}\bar{1}0 \rangle_{\alpha\text{-hex}}$ should be about three times larger than those of the other special boundaries, and the selected variants should grow extensively into not only one parent grain but also other grains in $\alpha\text{-hex(hexagonal)} \rightarrow \beta(\text{bcc})$ transformation. The model calculations of texture development during two consecutive cycles of $\alpha\text{-hex} \rightarrow \beta \rightarrow \alpha\text{-hex}$ transformation in CP-Ti and Zr are also shown.



Citation: Tomida, T.; Vogel, S.C.; Onuki, Y.; Sato, S. Texture Memory in Hexagonal Metals and Its Mechanism. *Metals* **2021**, *11*, 1653. <https://doi.org/10.3390/met11101653>

Academic Editor: David Field

Received: 11 September 2021

Accepted: 5 October 2021

Published: 18 October 2021

Keywords: texture memory; transformation texture; cubic; hexagonal; steel; titanium; zirconium

Publisher's Note: MDPI stays neutral with regard to jurisdictional claims in published maps and institutional affiliations.



Copyright: © 2021 by the authors. Licensee MDPI, Basel, Switzerland. This article is an open access article distributed under the terms and conditions of the Creative Commons Attribution (CC BY) license (<https://creativecommons.org/licenses/by/4.0/>).

1. Introduction

When materials transform from one phase to another and transform back to the initial phase, crystallographic textures in the initial phase are often retained to a great extent [1–7], and, in some cases, not only the textures but also the grain structures are reconstructed [8–10] despite diffusive transformation. These phenomena are called ‘texture memory’, and the latter are known as ‘austenite memory’ for fcc austenite (γ) \rightarrow martensite (or bainite) $\rightarrow \gamma$ transformation in steel [8–10]. Since the texture memory occurs in various industrial heating processes such as austenization in steel [1–3] as well as bcc β -phase heat treatment in Ti and Zr alloys [4–7] and influences many properties of the materials, studies on texture memory have been a central subject for decades in industry as well as academic fields.

For phase transformation in cubic and hexagonal metals, there are two well-known orientation relationships: the Kurdjumov–Sachs (K–S) orientation relationship in steel between

bcc α -ferrite (α -f) and γ , $\{111\}_\gamma // \{110\}_{\alpha-f}$, $\langle 1\bar{1}0 \rangle_\gamma // \langle 1\bar{1}1 \rangle_{\alpha-f}$, [11] and the Burgers orientation relationship (BOR) in e.g. Ti and Zr and their alloys between the low temperature hexagonal (α -hex) and high temperature β phases, $\{110\}_\beta // \{0001\}_{\alpha\text{-hex}}$, $\langle 1\bar{1}1 \rangle_\beta // \langle 2\bar{1}\bar{1}0 \rangle_{\alpha\text{-hex}}$, [12]. During phase transformation, orientations of parent phase grains are inherited to those of child phase grains by these orientation relationships. However, since multiple possible child orientations are allowed, of which the numbers are 24 for the K-S relation and 6 and 12 for BOR in $\alpha\text{-hex} \rightarrow \beta$ and $\beta \rightarrow \alpha\text{-hex}$, respectively, the texture in the initial phase would be largely smeared if all the variants were chosen at an equal rate. Nevertheless, texture memory occurs. Therefore, there must be some mechanisms that favor some orientation variants over others, i.e., variant selection, which has been thought to be responsible for the texture memory.

However, the mechanisms of variant selection are not thoroughly understood thus far [1–7], partly because of the difficulty of in situ observation of texture change during heat treatment at high temperatures, where oxidization of metal surfaces, grain growth and chemistry changes due to evaporation of elements take place easily. Recently, neutron and high-energy synchrotron X-ray diffractions by which bulk samples rather than only the sample surface can be characterized have become available for in situ high temperature texture measurements [4,5,7,13]. Additionally, electron back scattering diffraction (EBSD) analysis using scanning electron microscope (SEM) has enabled 2D [14,15] or even 3D micro-texture analysis [16–18], and thereby details of the texture changes during phase transformation have been revealed and the mechanisms behind them have gradually been clarified. The purpose of this articles is to explore the mechanisms of the texture memory in hexagonal metals, especially in pure Ti for which neutron diffraction data exist, and explain the observed texture evolution by the variant selection mechanism, which we call the double Burgers orientation relation (DBOR) where variants that hold BOR or near-BOR with two or more adjacent parent grains are selected.

2. Texture Memory in Ti and Zr Alloys

The texture memory in hexagonal metals such as commercially pure Ti (CP-Ti), Ti-6%Al-4%V and Zr-3%Nb is strong and often even strengthens their textures [4–7], which is one of the critical factors controlling various properties of the materials widely used in aerospace, chemical, biomedical, healthcare, and power generation industries [19–21]. Crystallographic textures that develop during thermomechanical processes in production cause large elastic, plastic, and thermal anisotropies [22] and are known to influence tensile strengths [22], fracture toughness [22–24], corrosion resistance, and biocompatibility [25,26] in the various industrial products.

The variant selection in hexagonal metals has been studied mostly for $\beta \rightarrow \alpha\text{-hex}$ transformation using β stabilized alloys, in which both product and parent phases of $\alpha\text{-hex}$ and β can be observed at room temperature. Furuhashi and his coworkers [27] reported by transmission electron microscopy that $\alpha\text{-hex}$ particles nucleated on β grain boundaries satisfied DBOR, which reduced interphase boundary energy. DBOR has been observed by several other investigations using EBSD [4,28]. Related to this mechanism, it is also well known that when two adjacent β grains nearly share a common $\{110\}$ plane (about 10° deviation allowed), $\alpha\text{-hex}$ variants often nucleate on the β grain boundary having the basal plane parallel to the common $\{110\}$ [28]. Inclination from grain boundary planes is also known to influence the variant selection such that the low energy facets of $\alpha\text{-hex}$ such as $\{112\}_\beta // \langle 1\bar{1}00 \rangle_{\alpha\text{-hex}}$ [29] or the common close-packed direction $\langle 111 \rangle_\beta // \langle 2\bar{1}\bar{1}0 \rangle_{\alpha\text{-hex}}$ [27] tend to be parallel to β grain boundary planes. Shi et al. proposed that DBOR was the first rule to be obeyed, and the second and the third were those related to the low energy facets [30]. However, it is not yet clear whether these mechanisms observed for individual grains can explain the bulk texture evolution during $\beta \rightarrow \alpha\text{-hex}$ transformation, partly because the mathematical basis to compute transformation textures based on the proposed mechanisms has not been established.

Another variant selection mechanism proposed for $\beta \rightarrow \alpha$ -hex transformation in Zrcalloy-4 was based on an anisotropic elastic energy stored in neighbor parent grains. Transformation strain of martensite (α' -hex) can cause elastic strain not only in a single parent grain but also in multiple parent grains, and the elastic anisotropy of the neighbor grains can cause differences in the elastic energy for different variants, i.e., variant selection. The texture of α' -hex was calculated based on the mechanism, and the reconstructed β texture from the observed α' -hex texture by EBSD agreed well with the observed α' -hex texture [6].

In situ texture measurements are best suited to investigating the high-temperature β textures. Lonardelli et al. [4] and Wenk et al. [5] have observed in situ the texture variations in CP-Ti and Zr (Zrcalloy-4), respectively, during α -hex \rightarrow β \rightarrow α -hex transformation cycles using a pulsed neutron diffractometer HIPPO in Los Alamos Neutron Science Center (LANSCE) [31,32]. They reported that the texture of α -hex that consists of components near $\{12\bar{1}5\}\langle 10\bar{1}0\rangle$ and $\{01\bar{1}3\}\langle 2\bar{1}\bar{1}0\rangle$ (transverse direction (TD)-split c-axis components) transformed to the β texture with a maximum around $\{112\}\langle 11\bar{1}\rangle$ (or components having $\langle 111\rangle$ along the rolling direction (RD)) with varying strengths of the cubic component $\{001\}\langle 100\rangle$. The cubic component in CP-Ti was as intense as the $\{112\}\langle 11\bar{1}\rangle$ component, whereas that in Zr was vanishingly small. These β textures were then observed to transform to α -hex textures with stronger near- $\{01\bar{1}3\}\langle 2\bar{1}\bar{1}0\rangle$ components than the initial texture, exhibiting the texture memory effect (see later sections for more details).

For the mechanism of the texture formation during α -hex \rightarrow β transformation, it has been proposed that the near- $\{01\bar{1}3\}\langle 2\bar{1}\bar{1}0\rangle$ components selectively transform in accordance with BOR and grow into the other components for both CP-Ti [4] and Zr [5]. A strong variant selection by an unknown mechanism was also required to explain the transformation textures [4]. Daymond et al. proposed a variant selection mechanism caused by stresses due to the anisotropy of thermal expansion in Zr-2.5%Nb, and qualitative agreement between observed and predicted β textures was reported [7]. Interestingly, DBOR has to the best of our knowledge never been proposed in α -hex \rightarrow β transformation, although DBOR has been suggested as a variant selection mechanism in $\beta \rightarrow \alpha$ -hex by many investigators. Therefore, open questions remain in the texture memory in hexagonal metals.

In the following sections, the mathematical basis to predict the α -hex $\beta \rightarrow$ and $\beta \rightarrow \alpha$ -hex transformation textures in hcp metals with variant selection, especially DBOR, is introduced. Then, we analyze the texture memory in α -hex \rightarrow $\beta \rightarrow \alpha$ -hex transformation in CP-Ti measured in situ via HIPPO in LANSCE [4,31,32], based on the mathematical basis described below.

3. Mathematical Basis of Transformation Texture Prediction for HCP Metals

3.1. Harmonic Equations for Transformation Texture Computation

Let us start with a very simple case, α -hex \rightarrow β transformation with only one variant. Given the rotation matrix for the orientation relationship, Δg , and the orientation distribution functions (ODF) of α -hex and β phases, $f_{\alpha\text{-hex}}(g)$ and $f_{\beta}(g)$, respectively, $f_{\beta}(g)$ is given by

$$f_{\beta}(g) = f_{\alpha\text{-hex}}(\Delta g^{-1} \cdot g). \quad (1)$$

When the orientation relation has a distribution of $w(\Delta g)$ as well as variants and a variant selection, $\rho(g)$, it follows that

$$f_{\beta}(g) = \oint w(\Delta g) \cdot \rho(\Delta g^{-1} \cdot g) \cdot f_{\alpha\text{-hex}}(\Delta g^{-1} \cdot g) d\Delta g. \quad (2)$$

with an appropriate symmetry operation, this equation gives transformation textures in which transformed components due to different variants are mixed as they naturally occur. The ODFs should have crystal and sample symmetries, $w(\Delta g)$ has the crystal symmetry of β phase, and $\rho(g)$ has sample symmetry [33].

We expand the above functions by generalized (symmetric) harmonics defined by Bunge [34] as follows:

$$f_{\alpha\text{-hex}}(g) = \sum_{\lambda=0}^{\infty} \sum_{\mu=1}^{M(\lambda)} \sum_{\nu=1}^{N(\lambda)} \alpha\text{-hex} C_{\lambda}^{\mu\nu} \cdot \overset{\cdot}{T}_{\lambda}^{\mu\nu}(g), \quad (3)$$

$$f_{\beta}(g) = \sum_{\lambda=0}^{\infty} \sum_{\mu=1}^{R(\lambda)} \sum_{\nu=1}^{N(\lambda)} \beta C_{\lambda}^{\mu\nu} \cdot \overset{\cdot\cdot}{T}_{\lambda}^{\mu\nu}(g), \quad (4)$$

$$w(g) = \sum_{\lambda=0}^{\infty} \sum_{\mu=1}^{R(\lambda)} \sum_{\nu=-\lambda}^{\lambda} w_{\lambda}^{\mu\nu} \cdot \overset{\cdot\cdot}{T}_{\lambda}^{\mu\nu}(g), \quad (5)$$

$$\rho(g) = \sum_{\lambda=0}^{\infty} \sum_{m=-\lambda}^{\lambda} \sum_{\nu=1}^{N(\lambda)} \rho_{\lambda}^{m\nu} \cdot \overset{\cdot}{T}_{\lambda}^{m\nu}(g), \quad (6)$$

where Ts are the generalized harmonic functions in which dots above indicate that symmetries of crystals and samples are included in the functions (three dots: β crystal symmetry, two dots: α -hex crystal symmetry, one dot: sample symmetry).

Then it follows that

$$\beta C_{\lambda}^{\mu\nu} = \frac{1}{2 \cdot \lambda + 1} \sum_{\lambda_1=0}^{\infty} \sum_{m=-\lambda_1}^{\lambda_1} \sum_{\nu_1=1}^{N(\lambda_1)} \sum_{\lambda_2=0}^{\infty} \sum_{\nu_2=1}^{N(\lambda_2)} \sum_{\mu_1=1}^{M(\lambda_1)} \sum_{s=-\lambda}^{\lambda} w_{\lambda}^{\mu s} \cdot \rho_{\lambda_2}^{r\nu_2, \alpha\text{-hex}} C_{\lambda_1}^{\mu_1\nu_1} \cdot \overset{\cdot\cdot}{A}_{\lambda_1}^{m\mu_1} \cdot (\lambda_1 \lambda_2 m r | \lambda s) \{ \lambda_1 \lambda_2 \nu_1 \nu_2 | \lambda \nu \}. \quad (7)$$

Here, $s = m + r$, $s \leq \lambda$ and $\overset{\cdot\cdot}{A}_{\lambda}^{m\mu}$, $(\lambda_1 \lambda_2 m r | \lambda s)$, and $\{ \lambda_1 \lambda_2 \nu_1 \nu_2 | \lambda \nu \}$ are the symmetry coefficients, the Clebsh–Goldan coefficients, and the generalized Clebsh–Goldan coefficients, respectively [34]. It is also held that $|\lambda_1 - \lambda_2| \leq \lambda \leq |\lambda_1 + \lambda_2|$. When there is no distribution in the orientation relation, Equation (7) can be written as

$$\beta C_{\lambda}^{\mu\nu} = \sum_{\lambda_1=0}^{\infty} \sum_{m=-\lambda_1}^{\lambda_1} \sum_{\nu_1=1}^{N(\lambda_1)} \sum_{\lambda_2=0}^{\infty} \sum_{\nu_2=1}^{N(\lambda_2)} \sum_{\mu_1=1}^{M(\lambda_1)} \sum_{s=-\lambda}^{\lambda} \overset{\cdot\cdot}{T}_{\lambda}^{\mu s*} (\Delta g) \cdot \rho_{\lambda_2}^{r\nu_2, \alpha\text{-hex}} C_{\lambda_1}^{\mu_1\nu_1} \cdot \overset{\cdot\cdot}{A}_{\lambda_1}^{m\mu_1} \cdot (\lambda_1 \lambda_2 m r | \lambda s) \{ \lambda_1 \lambda_2 \nu_1 \nu_2 | \lambda \nu \}. \quad (8)$$

In the analysis in the later sections, Equation (8) was used with BOR and the truncation at the order of 28th for λ and λ_1 and the 20th for λ_2 . The transformation texture for the reverse transformation from β to α -hex can be calculated in the same fashion.

3.2. DBOR

When a child phase nucleates on a grain boundary of a parent phase, the nucleus may hold an orientation relationship with not only one parent grain into which it grows but also one or more adjacent parent grains allowing a certain deviation from the orientation relation (up to around 10°) to further reduce interphase boundary energy. This hypothesis has been made for the transformation between α -f and γ in steel, called the double K-S relation (DKS) [3,35,36], and the texture prediction based on DKS has quantitatively explained various transformation textures such as those in hot-rolled steels [35,37] and texture memory effects in hot-rolled [3,14,36], cold-rolled [3], extruded [36], and ECAP(equal channel angular pressing)-processed [38] steels. DKS has been experimentally observed by 2D- [14,15] and 3D-EBSD [16,17] as well as 3D synchrotron X-ray measurement recently [39]. This concept is an extension of the mechanism proposed by Hutchinson and Kestens [2] and Yoshinaga et. al. [40], which have been published in the same narrow period. The mechanism called DKS is extended to include not only the rare case of grain boundaries in which the variants of the original orientations exactly satisfy the rule but also other boundaries for which many variants can hold the DKS relation with the deviation up to about 10° . Then DKS can be applied to both for α -f \rightarrow γ and $\gamma \rightarrow$ α -f transformations explaining the observed texture memory as well as the transformation textures in hot-rolled steel, and, more importantly, this generalized mechanism allows us to accurately predict the transformation textures in steels of this kind.

Here, we adapt the mathematical scheme of DKS for fcc/bcc transformations [3,36] to DBOR for hexagonal metals exhibiting hcp/bcc transformations. Let us assume α -hex \rightarrow β transformation for the mathematical formulation. A growing β nucleus satisfies DBOR when two neighboring parent grains satisfy $g_2 \approx \Delta g_k^{-1} \cdot \Delta g_i \cdot g_1$, as shown in Figure 1a. In this equation, g_1 and g_2 are the orientations of the two adjacent parent grains, α_1 and α_2 , and Δg_i and Δg_k are possible BOR variants (rotation matrices) for α_1 and α_2 . Note that if Δg_i is crystallographically equivalent to Δg_k , α_1 and α_2 have the same orientation; therefore, the grain boundary is absent, in which case it should be omitted.

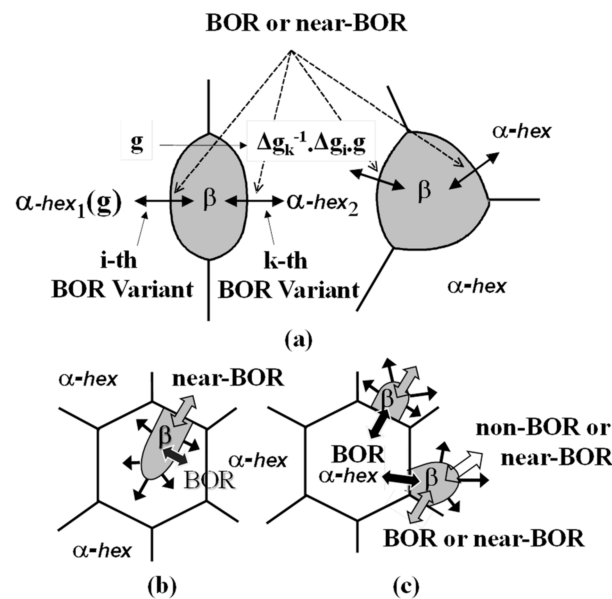


Figure 1. Schematic representations of (a) nucleation of DBOR variants and (b) growth by coherent interfaces and (c) semi-coherent or incoherent interfaces of selected variants by DBOR in α -hex \rightarrow β transformation. EDBOR growth can occur by mobile semi-coherent and incoherent interfaces.

It is also important to note that the grain boundaries on which nuclei can hold DBOR are always specific (or special) types of boundaries, as listed in Table 1, or close to them. We may consider different nucleation rates, ζ , for different types of special boundaries including $\zeta = 0$ for the above “boundary-less” case.

Table 1. Special boundaries for DBOR and $\delta r_m / \delta \zeta$ and optimum ζ for predictions by EDBOR $n = 1$ scheme.

Phase Transformation	Type	Rotation Between Adjacent Grains			Number Ratio	$\delta r_m / \delta \zeta$ (10^{-2})	Optimum ζ
		Angle	Axis	Deviation from $\langle 2110 \rangle$			
α -hex \rightarrow β	I	10.5°	c-axis	90°	1	−0.4	1
	II	60°	$\langle 2\bar{1}\bar{1}0 \rangle$	0°	2	2.9	1
	III	60.8°	$\langle 7431 \rangle$	10.4°	4	4.9	1
	IV	63.3°	$\langle 42\bar{2}1 \rangle$	17.6°	2	3.4	1
	V	90°	$\langle 74\bar{3}0 \rangle$	5.3°	2	−7.2	3
$\beta \rightarrow \alpha$ -hex	I	10.5°	$\langle 110 \rangle$	—	1	2.7	0
	II	49.5°	$\langle 110 \rangle$	—	1	−7.1	3
	III	60°	$\langle 111 \rangle$	—	1	−3.4	1
	IV	60°	$\langle 110 \rangle$	—	2	−7.9	1

The probability for the i -th variant to be chosen, $\rho_i(g)$, may be proportional to the orientation density of the parent phase around $\Delta g_k^{-1} \cdot \Delta g_i \cdot g$, since the i -th variant needs

a parent grain of the orientation around $\Delta g_k^{-1} \cdot \Delta g_i \cdot g$ on the opposite side of the grain boundary to satisfy DBOR,

$$\rho_i(g) \propto \sum_k f_{\alpha-hex} \left(\Delta g_k^{-1} \cdot \Delta g_i \cdot g \right). \quad (9)$$

Introducing the variable ω that determines the intensity of variant selection and the material conservation law, the probability function shown below can be derived:

$$\rho(g) = \frac{\omega}{N_k \cdot \bar{\zeta}} \cdot \sum_{k=1}^{N_k} \zeta_k \cdot f_{\alpha-hex} \left(\Delta g^{-1} \cdot g_k^c \cdot \Delta g \cdot g \right) + \rho_C(g), \quad (10)$$

$$\rho_C(g) = 1 - \frac{\omega}{N_i \cdot N_k \cdot \bar{\zeta}} \cdot \sum_{i=1}^{N_i} \sum_{k=1}^{N_k} \zeta_k \cdot f_{\alpha-hex} \left(\Delta g^{-1} \cdot g_k^c \cdot \Delta g \cdot g_i^h \cdot g \right). \quad (11)$$

Here, g_i^h , g_k^c , N_i , and N_k are the rotational operators for the hexagonal and cubic crystal symmetries and the numbers of operators (12 and 24 for hexagonal and cubic symmetries), respectively. Note that the $\Delta g \cdot g_i^h \cdot g$ represents the i -th BOR variant for α -hex \rightarrow β with the only orientation relation for BOR, Δg . Although the number of the symmetry operations in hexagonal crystals is 12, the number of variants in α -hex \rightarrow β in BOR is 6 because of the symmetry of BOR; this redundancy is two for both α -hex \rightarrow β and β \rightarrow α -hex. Therefore, the variant selection function $\rho(g)$ has different values for the crystallographically equivalent 12 orientations in the parent α -hex phase and holds the symmetry of samples. In Equations (10) and (11), the nucleation rates ζ_k for the special boundaries, the type of which is determined by g_k^c , are included.

The first term of Equation (10) is the term for the selection by the DBOR mechanism, while the second term is for the case where the selection by DBOR does not occur, since when $\omega \rightarrow 0$, the second term only determines the variant selection. The second term in Equation (11) means “no variant selection”. Therefore, roughly speaking, ω is the fraction of the parent phase which obeys DBOR during transformation, and for the rest, $1-\omega$ transforms without variant selection.

Equations (10) and (11) can be expanded by the generalized spherical harmonics with the coefficients:

$$\rho_\lambda^{mv} = \frac{\omega}{N_i \cdot N_k \cdot \bar{\zeta}} \sum_{\mu=1}^{M(\lambda)} \alpha^{-hex} C_{\lambda}^{\mu\nu} \cdot \sum_{i=1}^{N_i} \sum_{k=1}^{N_k} \zeta_k \cdot \left[\dot{T}_{\lambda}^{\mu m} \left(\Delta g^{-1} \cdot g_k^c \cdot \Delta g \right) - \dot{T}_{\lambda}^{\mu m} \left(\Delta g^{-1} \cdot g_k^c \cdot \Delta g \cdot g_i^h \right) \right] \quad (12)$$

and

$$\rho_0^{0,1} = 1. \quad (13)$$

3.3. Extended Concept of Double BOR (EDBOR)

The above equations, Equations (10)–(13), for DBOR satisfy local as well as global material conservation during transformation. The local material conservation means that the volume of a parent crystal is conserved during the transformation and equal to the total volume of the related child grains by BOR, which occurs when nuclei grow by the migration of coherent interfaces, as shown Figure 1b, like martensite transformation. This is because Equation (11) ensures that the average of $\rho(g)$ for all the 6 variants (12 equivalent parent orientations) is always unity,

$$\frac{1}{N_i} \sum_{i=1}^{N_i} \rho \left(g_i^h \cdot g \right) = 1, \quad (14)$$

and the global or whole material volume is also conserved during the transformation. Therefore,

$$\beta C_0^{1,1} = 1 \text{ in Equations (7) and (8)} \quad (15)$$

The local volume conservation, which strictly occurs for martensite transformation, is a reasonably good approximation for diffusional transformation, and it has been successfully used in the predictions of various transformation textures in steels as mentioned above [3,35–38].

However, the growth of nuclei during diffusional or reconstructive transformation may not occur by the migration of coherent interfaces, rather it can occur towards neighbor grains to which growth fronts are incoherent or semi-coherent, as shown in Figure 1c, and the growth may not be confined within one parent grain [36]. This can be caused by higher mobility of the incoherent interphase boundaries [17]. In an oxide dispersed steel (ODS) steel, this type of growth explained the observed strong texture memory effect well [13,36].

To model this type of growth, the second term of Equations (10) and (11) should be modified. Since the second term is for the case where variant selection does not obey DBOR with no variant selection rule, Equation (10) may be rewritten with a “constant δ ” as the second term as follows:

$$\rho(g) = \frac{\omega}{N_k \cdot \bar{\zeta}} \cdot \sum_{k=1}^{N_k} \zeta_k \cdot f_{\alpha-hex} \left(\Delta g^{-1} \cdot g_k^c \cdot \Delta g \cdot g \right) + \delta. \quad (16)$$

By using the constant δ , the growth is no longer limited within one parent grain. To further extend this idea for the case where a very strong variant selection occurs, non-linear probability proportional to the n -th power of $f(\Delta g^{-1} \cdot g_k^c \cdot \Delta g \cdot g)$ can be introduced as

$$\rho(g) = \omega \cdot \left\{ \frac{1}{N_k \cdot \bar{\zeta}} \cdot \sum_{k=1}^{N_k} \zeta_k \cdot f_{\alpha} \left(\Delta g^{-1} \cdot g_k^c \cdot \Delta g \cdot g \right) \right\}^n + \delta. \quad (17)$$

For $n = 1$, its expansion coefficients by harmonics are expressed as

$$\rho_{\lambda}^{mv} = \frac{\omega}{N_k \cdot \bar{\zeta}} \sum_{\mu=1}^{M(\lambda)} \alpha-hex C_{\lambda}^{\mu\nu} \sum_{k=1}^{N_k} \zeta_k \cdot T_{\lambda}^{\mu m} \left(\Delta g^{-1} \cdot g_k^c \cdot \Delta g \right), \quad (18)$$

$$\rho_0^{0,1} = \omega + \delta. \quad (19)$$

Now, the coefficients ${}^{\beta}C_{\lambda}^{\mu\nu}$ obtained from Equations (7) or (8) are functions of ω and δ . Since the global volume conservation must also be fulfilled in this case, δ should be a function of ω determined by Equation (15). Since δ is constant, it follows that

$${}^{\beta}C_{\lambda}^{\mu\nu}(\omega, \delta) = {}^{\beta}C_{\lambda}^{\mu\nu}(\omega, 0) + \delta \cdot {}^{\beta}C_{\lambda}^{\mu\nu}(0, 1). \quad (20)$$

Then, to satisfy Equation (15),

$${}^{\beta}C_0^{1,1}(\omega, \delta) = {}^{\beta}C_0^{1,1}(\omega, 0) + \delta \cdot {}^{\beta}C_0^{1,1}(0, 1) = 1. \quad (21)$$

Therefore, since ${}^{\beta}C_0^{1,1}(0, 1) = 1$, the value of δ is determined as

$$\delta = 1 - {}^{\beta}C_0^{1,1}(\omega, 0). \quad (22)$$

Hence, from Equations (20) and (22), it follows that

$${}^{\beta}C_{\lambda}^{\mu\nu}(\omega) = {}^{\beta}C_{\lambda}^{\mu\nu}(\omega, 0) + {}^{\beta}C_{\lambda}^{\mu\nu}(0, 1) \cdot (1 - {}^{\beta}C_0^{1,1}(\omega, 0)). \quad (23)$$

Therefore, by computing ${}^{\beta}C_{\lambda}^{\mu\nu}$ in two cases, a given value of ω and $\delta = 0$ and $\omega = 0$ and $\delta = 1$ (no variant selection) using Equations (8) or (7), (18) and (19), the transformation texture that satisfies EDBOR ($n = 1$) as well as the global volume conservation can be

obtained. For EDBOR of $n > 1$, a theorem for the product of two harmonics [33], shown below, can be used to calculate the expansion coefficients of the $\rho(g)$:

$$\dot{T}_{\lambda_1}^{mv_1}(g)\dot{T}_{\lambda_2}^{rv_2}(g) = \sum_{\lambda=|\lambda_2-\lambda_1|}^{|\lambda_2+\lambda_1|} \sum_{\nu=1}^{N(\lambda)} (\lambda_1\lambda_2mrv|\lambda s)\{\lambda_1\lambda_2\nu_1\nu_2|\lambda\nu\}\dot{T}_{\lambda}^{sv}(g), \quad (24)$$

where $s = m + r$.

For example, when $n = 2$, using the expansion coefficients of $\frac{1}{N_k\bar{\zeta}} \sum_k \zeta_k \cdot f(\Delta g^{-1} \cdot g_k^c \cdot \Delta g \cdot g)$,

$$\Sigma f_{\lambda}^{mv} = \frac{1}{N_k\bar{\zeta}} \sum_{\mu=1}^{M(\lambda)} a\text{-hex} C_{\lambda}^{\mu\nu} \sum_{k=1}^{N_k} \zeta_k \cdot \dot{T}_{\lambda}^{\mu m}(\Delta g^{-1} \cdot g_k^c \cdot \Delta g), \quad (25)$$

it follows that

$$\rho_{\lambda}^{sv} = \omega \cdot \sum_{\lambda_1=0}^{\infty} \sum_{\lambda_2=0}^{\infty} \sum_{m=-\lambda_1}^{\lambda_1} \sum_{\nu_1=1}^{N(\lambda_1)} \sum_{\nu_2=1}^{N(\lambda_2)} (\lambda_1\lambda_2mrv|\lambda s)\{\lambda_1\lambda_2\nu_1\nu_2|\lambda\nu\} \cdot \Sigma f_{\lambda_1}^{mv_1} \cdot \Sigma f_{\lambda_2}^{rv_2} \quad (26)$$

here, $s = m + r$, and $|\lambda_1 - \lambda_2| \leq \lambda \leq |\lambda_1 + \lambda_2|$.

Then, the rest is the same as Equations (20)–(23). In this study, Equations (12), (13), (18), (19) and (26) were used with the truncation at the 20th order to roughly simulate the allowed deviation of Δg^{-1} around 10° . DBOR and EDBOR for the reversed transformation from β to α -hex were formulated in the same fashion.

It should be emphasized that for DBOR and EDBOR, the variant selection is determined by the texture of parent phases, and the stronger the texture of parent phases, the stronger the variant selection occurs for the transformation. For simple DBOR in Section 3.2, an ideal case explained above is attained with $\omega = 1$. However, for EDBOR, this physical meaning of ω would be lost, especially for $n = 2$ or higher. For DKS in steel, the value of ω has been reported to vary from 0.5 to even greater than unity [3,35–38]. Therefore, the value of ω is dependent on grain structures, on which the probability by which DBOR variants can exist is dependent, and, of course, the order of n in EDBOR.

4. Experimental Procedure

Texture change of cold-rolled CP-Ti (ASTM grade 2) was observed in situ during an α -hex \rightarrow β \rightarrow α -hex heating cycle by a time-of-flight pulsed neutron diffractometer HIPPO in LANSCE [4,31,32]. Details are given in [4] and only a summary of the experiment is provided here. A $5 \times 5 \times 5 \text{ mm}^3$ cube sample cut from the 5 mm thick cold-rolled sheet was slowly heated up to β transformation temperature of 950°C in vacuum step-wise, as shown in Figure 2, and textures were measured at each heat step. In this study, the data taken at 800°C before phase transformation, at 950°C for high temperature β , and at 400°C for final α after the heating cycle, were used. No diffraction of α -hex phase was observed at 950°C . The grain structure before transformation was relatively fine around $20 \mu\text{m}$ in grain size. However, grains were coarsened to about 1 mm during the heating.

The neutron diffraction spectra were analyzed by the Rietveld method [41] implemented in the software package MAUD [42]. During the Rietveld analysis, textures were analyzed based on a discrete E-WIMV method [43] implemented in MAUD. These obtained data have been already published, and thus the readers may refer to the literature for further details [4]. The recalculated pole figures from the E-WIMV representation of ODFs were used to obtain harmonic-expanded ODFs [34] to utilize the above method for transformation texture prediction. A method described in [34] and the Standard ODF software [44] were used for the harmonic expansion for α -hex and β phases using 10 and 4 complete pole figures, respectively. During the harmonic expansion, the orthorhombic sample symmetry was applied. The expansion was truncated at the 28th and 22nd orders for α -hex and β , respectively, which was determined considering sharpness of the observed

textures. The crystal coordinates and Euler angles used in this study were those defined by Bunge et. al., i.e., x-axis// $[10\bar{1}0]$ and y-axis// $[\bar{1}2\bar{1}0]$ for α -hex [34].

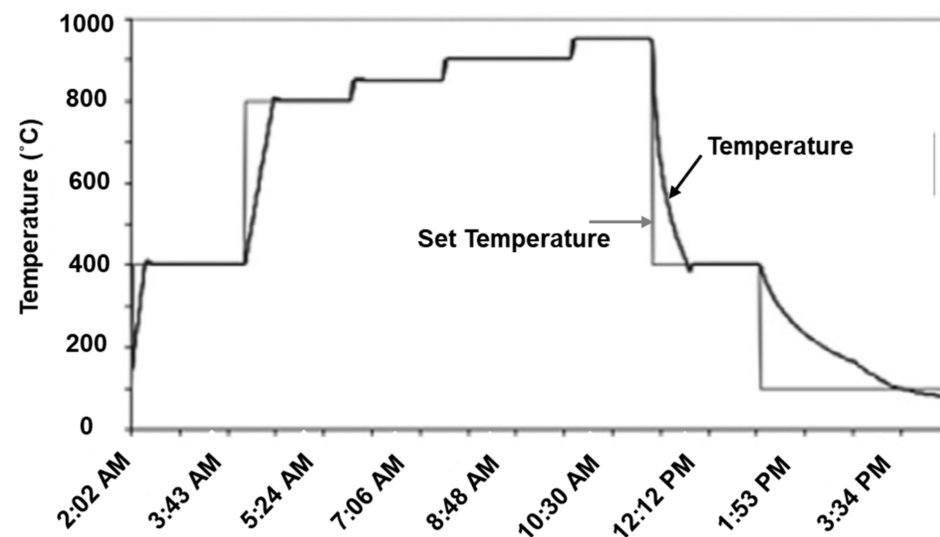


Figure 2. Heating pattern of in situ observation of textures in CP-Ti by HIPPO [4]. The data used in this study are those at 800 °C before transformation, at 950 °C after α -hex $\rightarrow\beta$ transformation, and at 400 °C after the heating cycle.

5. Experimental Results and Prediction by DBOR

5.1. Experimental Results

Figures 3 and 4 show the ODF sections and recalculated pole figures of α -hex and β phases observed at 800, 950, and 400 °C. It is seen that the initial texture before transformation at 800 °C is composed of TD-split c-axis components, of which the inclination angle of the c-axis from ND is about 35°. As seen in Figure 3a, these TD-split components form a fiber lying from $\{\bar{1}2\bar{1}5\}\langle 10\bar{1}0\rangle$ to $\{01\bar{1}3\}\langle 2\bar{1}\bar{1}0\rangle$ as often observed for recrystallized Ti after cold-rolling [22]. The intensity of the $\{\bar{1}2\bar{1}5\}\langle 10\bar{1}0\rangle$ component, which is in general dominant in cold-rolled states [4], was slightly weaker than the $\{01\bar{1}3\}\langle 2\bar{1}\bar{1}0\rangle$ component. The recrystallized α -hex then transformed to β , the texture of which consists of only two components, the cubic $\{001\}\langle 100\rangle$ and $\{112\}\langle 11\bar{1}\rangle$ orientations. The cubic component was the strongest in ODF density, while the $\{112\}\langle 11\bar{1}\rangle$ component had a larger volume because of multiplicity.

As seen in Figures 3c and 4g–i, the final α -hex texture had sharper and stronger TD-split c-axis components than the initial α texture, for which the inclination angle was also about 35°. Thus, the texture memory effect was clearly observed. However, the TD split components in the final α -hex were more dominated by $\{01\bar{1}3\}\langle 2\bar{1}\bar{1}0\rangle$ than $\{\bar{1}2\bar{1}5\}\langle 10\bar{1}0\rangle$ unlike the initial α -hex. In addition, there were “RD”-split c-axis components around $\{\bar{1}2\bar{1}3\}\langle 1\bar{2}12\rangle$, for which the inclination angle from ND was about 45°. Another sub-component was also seen around $\{\bar{1}2\bar{1}0\}\langle 10\bar{1}1\rangle$, in which the c-axis lay in the sheet plane along the direction of 45° to RD.

5.2. Prediction Results by DBOR

5.2.1. α -hex $\rightarrow\beta$ Transformation

β textures were computed using the observed α texture before transformation shown in Figures 3a and 4a–c and the mathematical method explained above, and they were compared to the observed β texture. As shown in Figure 5, root mean square (RMS) minimization was performed between the observed and predicted ODFs changing the value of ω as a parameter. For simple DBOR by Equations (10) and (11), the RMS deviation (rm) showed a minimum around $\omega = 0.7$. However, the reduction in the deviation (difference in

rm between arrows a and b in Figure 5) was not significant. In contrast, the deviation was significantly reduced by EDBOR (see arrows c and d in Figure 5).

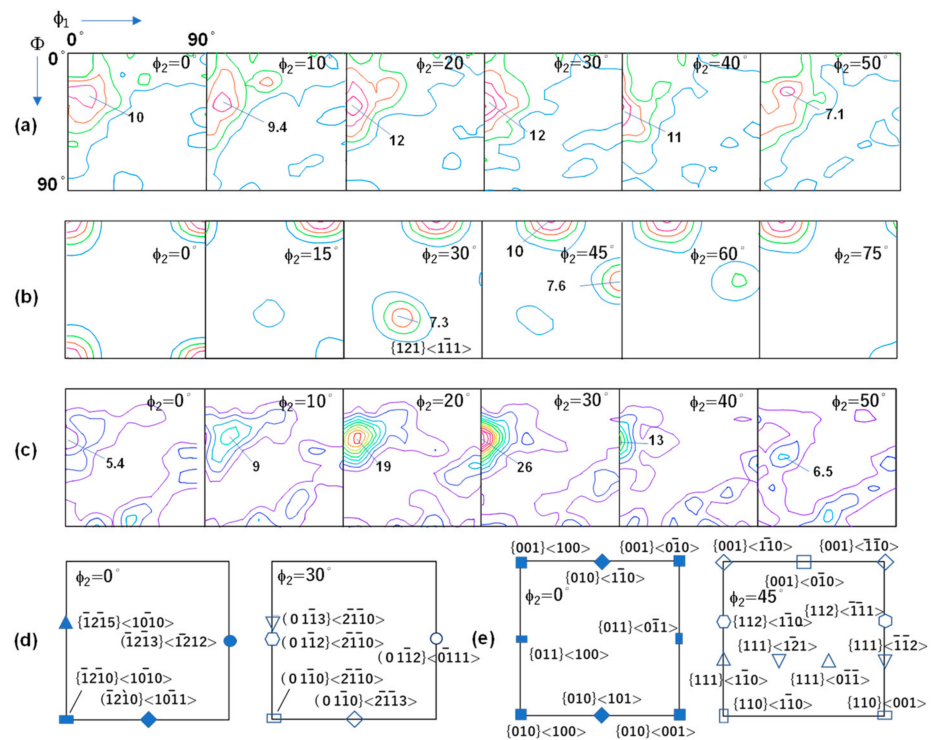


Figure 3. ODF sections of observed textures of CP-Ti, (a) initial α -hex at 800 °C, (b) β at 950 °C, (c) α -hex after transformation cycle at 400 °C, and (d,e) important orientations in α -hex and β , respectively. Contour levels are 2, 4, 6.

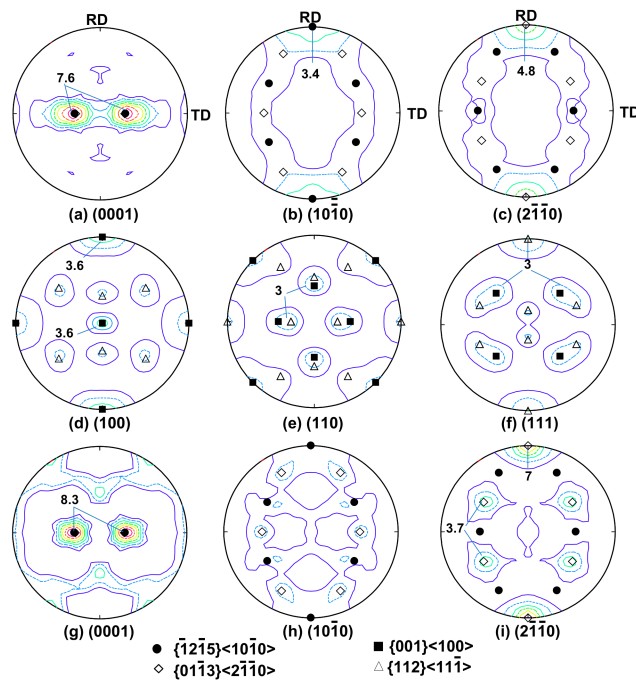


Figure 4. Pole figures of observed textures of CP-Ti, (a–c) initial α -hex at 800 °C, (d–f) β at 950 °C, and (g–i) α -hex at 400 °C after transformation cycle. Contour levels are 1, 2, 3.

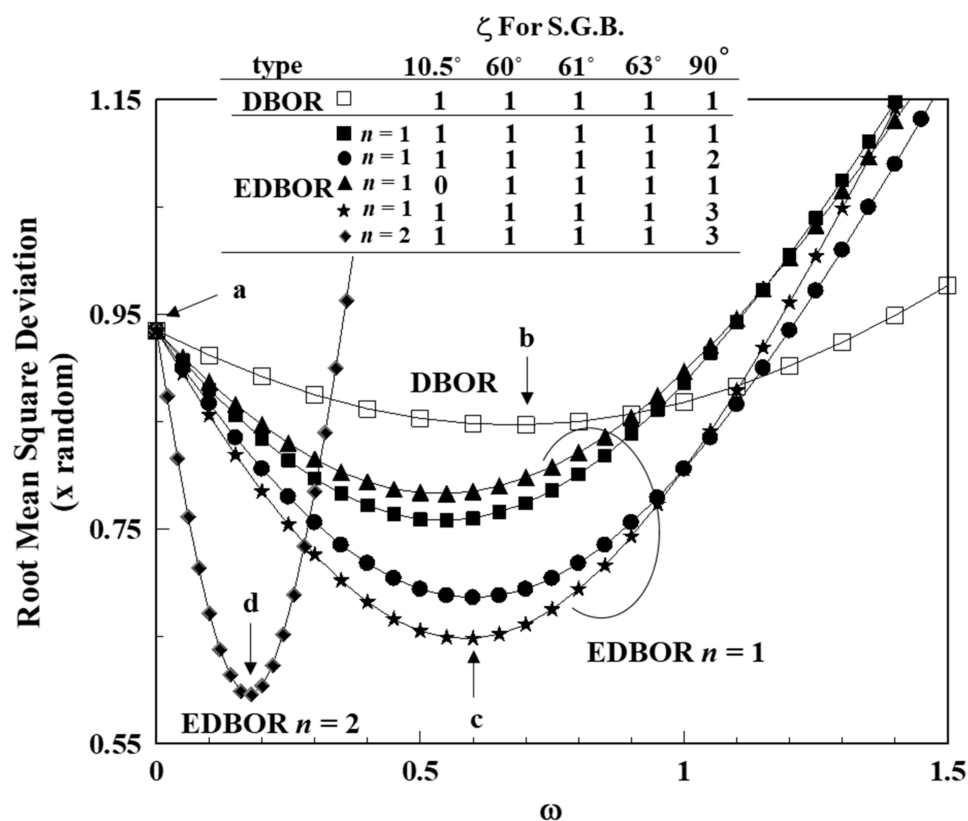


Figure 5. Change in root mean square deviation between observed and predicted ODFs by changing ω and ζ . See inset table for calculation conditions.

Following the determination of ω , via EDBOR $n = 1$, the influence of nucleation rates ζ for special boundaries was investigated. As listed in Table 1, there are five kinds of special grain boundaries of DBOR in α -hex \rightarrow β transformation. For each type of grain boundary, the change in the rm at the optimum ω was calculated by changing ζ independently from one to two. This change $\delta\text{rm}/\delta\zeta$, which is the gradient of rm when increasing each weight factor, is listed in Table 1. The $\delta\text{rm}/\delta\zeta$ for 10.5° small-angle boundaries was small and negative, those for 60, 60.8 and 63.3° boundaries were close to each other considering their number ratios (1:2:1) and positive, and those for 90° boundaries were largely negative. Therefore, when decreasing ζ for the small-angle boundaries, rm slightly increased, and when increasing ζ for the 90° boundaries, rm significantly reduced, as shown in Figure 5. Therefore, the determined optimum ratios of ζ for 10.5, 60, 60.8, 63.3, 90° boundaries are 1:1:1:1:3; note that only rough optimization of ζ was performed since a full optimization would require many more observations.

In Figure 6a–d, the change in $\varphi_2 = 45^\circ$ sections of ODF by the above optimization is shown. Although the prediction without variant selection resulted in a significantly weaker texture than the observed one, DBOR predicted the proper intensity of the texture. With equal values of ζ for all the types of special boundary, the $\{001\}\langle 100\rangle$ cubic component was predicted to be somewhat weaker than the observation (see Figure 6b). However, by increasing the value of ζ for the 90° special boundary, the intensity of the cubic component increased, and the optimal prediction was obtained by EDBOR $n = 2$, as shown in Figure 6d–h (see also arrow d in Figure 5). The predicted ODF and pole figures agreed remarkably well with the observed ones as shown in Figures 3b and 4d–f.

Variant selection probabilities $\rho(g)$ for typical parent orientations for the optimal predictions by EDBOR $n = 1$ and 2 are shown in Figure 7. Note that the value of $\rho(g)$ is unity without variant selection, and the averaged ρ for variants, $\bar{\rho}$, is also unity when the local volume is conserved. The child orientations of variants are listed in Table 2. It is seen in Figure 7 that the ρ for the $\{01\bar{1}3\}\langle 2\bar{1}10\rangle$ and $\{01\bar{1}2\}\langle 2\bar{1}10\rangle$ parent orientations to

transform to the child orientations $g_{\beta}1s$, which were around $\{112\}\langle 11\bar{1}\rangle$ and $\{001\}\langle 100\rangle$, respectively (see Table 2), was relatively large. Furthermore, the $\bar{\rho}$ for these parent orientations was 1.5 to 1.7, meaning these orientations grow beyond the limit of the local volume conservation. However, the values of ρ as well as $\bar{\rho}$ of the $\{\bar{1}2\bar{1}5\}\langle 10\bar{1}0\rangle$ parent orientation were all smaller than unity. Therefore, the variants from the $\{01\bar{1}3\}\langle 2\bar{1}\bar{1}0\rangle$ and $\{01\bar{1}2\}\langle 2\bar{1}\bar{1}0\rangle$ parent orientations, known as the growth components, preferentially nucleated and grew over multiple parent grains, whereas the volume inherited from the $\{\bar{1}2\bar{1}5\}\langle 10\bar{1}0\rangle$ orientation shrank. The predicted total volume of the child orientations of $\{01\bar{1}3\}\langle 2\bar{1}\bar{1}0\rangle$ was 1.5 to 1.7 times of the volume of the parent orientation, whereas that of $\{\bar{1}2\bar{1}5\}\langle 10\bar{1}0\rangle$ was only 0.77 times of the volume of the parent orientation.

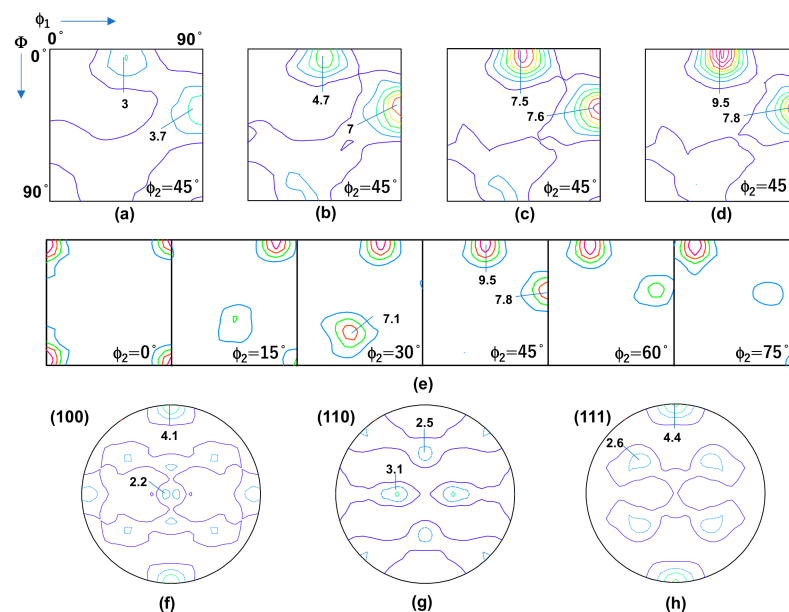


Figure 6. (a–d) ODF $\varphi_2 = 45^\circ$ sections for predictions of β textures (a) without and (b–d) with variant selection. The conditions of prediction in Figure 6a–d are indicated by arrows a–d in Figure 5, respectively. (e) and (f–h) ODF sections and pole figures for the optimum prediction by EDBOR $n = 2$ shown in Figure 6d. Contour levels are (a–d) and (f–h) 1, 2, 3... and (e) 2, 4, 6..., respectively.

Table 2. Orientations of major components in observed textures and their BOR and DBOR variants on the special boundaries. Three angles separated by slashes are Euler angles, $\varphi_1/\Phi/\varphi_2$. Bold letters indicate DBOR variants, and ** and * indicate exact and near-DBOR variants on typical grain boundaries, respectively. Note that the number of BOR variants reduces to three or 7 by symmetry of parent orientations.

Type	$\alpha\text{-hex}\rightarrow\beta$			$\beta\rightarrow\alpha\text{-hex}$			
Parent O.R.	$\{0113\}\langle 2110\rangle$ 0°/31°/30°	$\{0112\}\langle 2110\rangle$ 0°/43°/30°	$\{\bar{1}215\}\langle 1010\rangle$ 0°/33°/0°	$\{001\}\langle 100\rangle$ 0°/0°/0°	$\{\bar{1}12\}\langle \bar{1}11\rangle$ 90°/35°/45°		
Typical special G.B.	2° from II between TD-split pair	4° from V between TD-split pair	None	16° from IV between {001}<100> & {112}<111>	III between symmetry pair & 16° from IV between {001}<100> & {112}<111>		
Child O.R. of BOR	$g_{\beta}1$	$\{112\}\langle 11\bar{1}\rangle$ *	$\{001\}\langle 100\rangle$ *	$\{113\}\langle 21\bar{1}\rangle$	$g_{\alpha\text{-hex}}1$	$\{01\bar{1}2\}\langle 2\bar{1}\bar{1}0\rangle$ *	$\{01\bar{1}3\}\langle 2\bar{1}\bar{1}0\rangle$ **,*
	$g_{\beta}2$	$\{014\}\langle 100\rangle$	$\{853\}\langle \bar{1}\bar{1}\bar{1}\rangle$	$\{111\}\langle 0\bar{1}\bar{1}\rangle$	$g_{\alpha\text{-hex}}2$	$\{\bar{1}210\}\langle 10\bar{1}\bar{1}\rangle$	0°/30°/19.5° *
	$g_{\beta}3$	$\{447\}\langle 43\bar{4}\rangle$	$\{376\}\langle 3\bar{3}2\rangle$	$\{114\}\langle 31\bar{1}\rangle$	$g_{\alpha\text{-hex}}3$	$\{01\bar{1}2\}\langle 0\bar{1}\bar{1}1\rangle$	$\{01\bar{1}0\}\langle 2\bar{1}\bar{1}0\rangle$ **
					$g_{\alpha\text{-hex}}4$		$\{\bar{1}213\}\langle \bar{1}2\bar{1}2\rangle$
					$g_{\alpha\text{-hex}}5$		0°/90°/19.5°
					$g_{\alpha\text{-hex}}6$		59°/83°/0.5°
					$g_{\alpha\text{-hex}}7$		59°/83°/10°

** : Exact DBOR variant, * : near-DBOR variant, bold letter: DBOR variants.

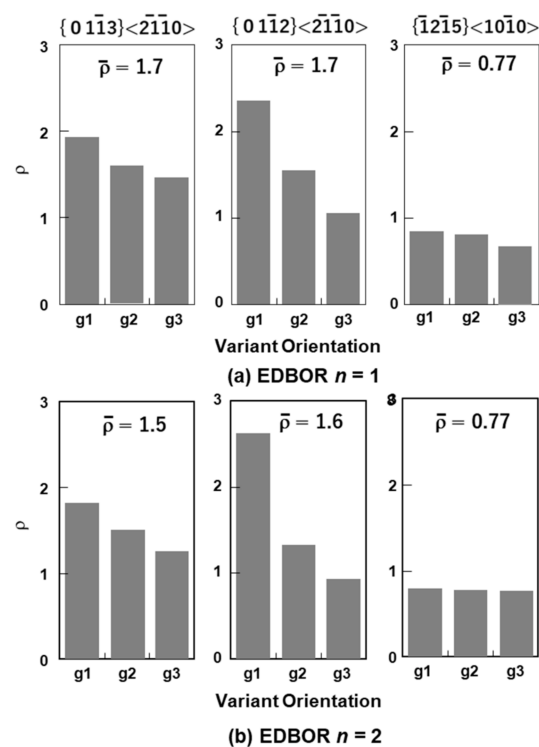


Figure 7. Variant selection probability, ρ , for parent orientations $\{01\bar{1}3\}\langle 2\bar{1}10\rangle$, $\{01\bar{1}2\}\langle 2\bar{1}10\rangle$ and $\{\bar{1}2\bar{1}5\}\langle 10\bar{1}0\rangle$ in optimum predictions by (a) EDBOR $n = 1$ and (b) EDBOR $n = 2$, shown in Figure 6c–h for α -hex \rightarrow β transformation. The conditions for optimum predictions are indicated by arrows c and d in Figure 5. See Table 2 for variant orientations.

5.2.2. $\beta \rightarrow \alpha$ -hex Transformation

Textures of α -hex were computed using the observed β texture at 950 °C and the mathematical method explained above, and they were compared to the observed α -hex texture at 400 °C after the heating cycle. As shown in Figure 8, RMS minimization was performed as explained above, and the $\delta_{rm}/\delta\zeta$ for four kinds of special grain boundaries in α -hex transformation listed in Table 1 was also calculated using EDBOR $n = 1$. Agreement between predicted and observed α -hex textures was greatly improved by DBOR as well as EDBOR by choosing proper values of ω . The values of $\delta_{rm}/\delta\zeta$ were positive for 10.5° small-angle boundaries, negative for the other types of boundaries, and smallest for 49° boundaries considering the ratio of grain boundary numbers, 1:1:1:2 for 10.5°, 49.5°, $\Sigma 3$, and 60° $\langle 110 \rangle$. Therefore, the agreement was improved by decreasing ζ for the small-angle boundaries and increasing ζ for the 49.5° boundaries. Hence, the optimum prediction was obtained with the ratio of ζ , roughly 0:3:1:1 for 10.5°, 49.5°, $\Sigma 3$, and 60° $\langle 110 \rangle$ boundaries, and, unlike the α -hex \rightarrow β transformation, EDBOR did not greatly improve the prediction in comparison to DBOR (see arrows b and c in Figure 8). It is noteworthy that with all the ζ s as unity (as well as even $\omega = 1$), DBOR gave a good agreement to the observed α -hex texture, as shown by open squares in Figure 8.

Figure 9a–d illustrate how DBOR and EDBOR improve the prediction. Without variant selection, the predicted α -hex texture was significantly weaker than the observed texture, indicating strong variant selection operating in $\beta \rightarrow \alpha$ -hex transformation in CP-Ti. With the variant selection by DBOR and EDBOR, the intensity of the texture greatly increased and became closer to the observed one. It was also seen that the difference between the predictions by DBOR and EDBOR was negligible, as mentioned above (see Figure 9b,c). As seen in Figure 9c–h, the optimum prediction reproduced all the important features of the observed texture of α -hex after the heating cycle. The same was true for the prediction based on the “predicted β texture” in Figure 6d–h, as seen in Figure 9d.

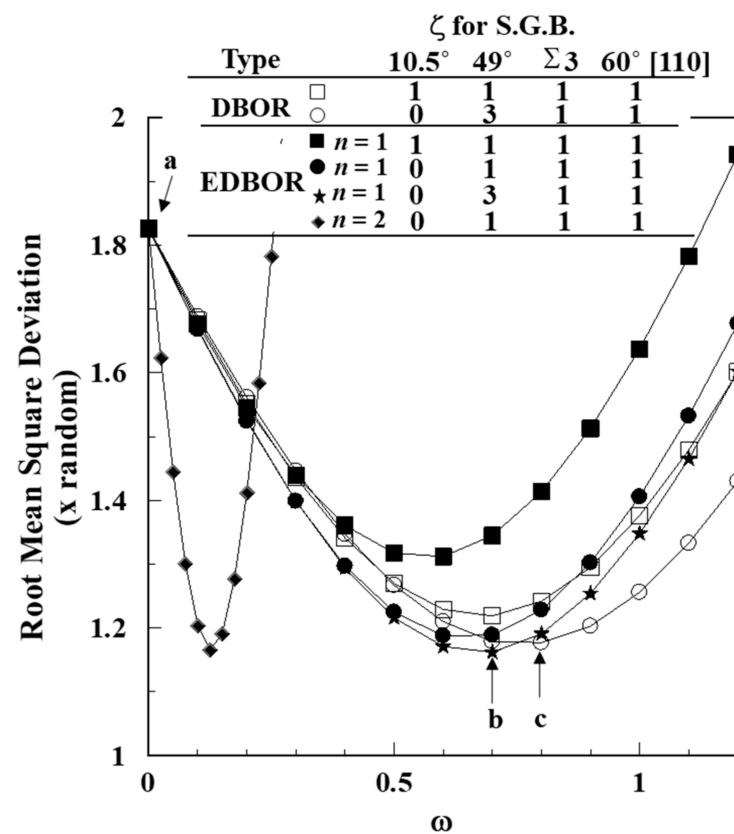


Figure 8. Change in root mean square deviation between observed and prediction ODFs by changing ω and ζ for $\beta \rightarrow \alpha$ -hex transformation. See inset table for calculation conditions.

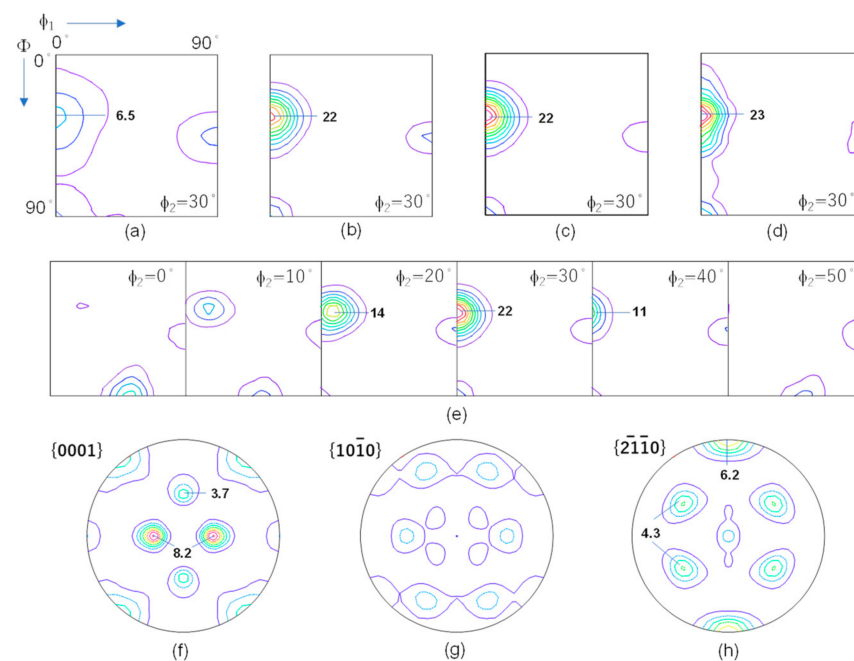


Figure 9. (a–d) ODF $\varphi_2=30^\circ$ sections for predictions of β textures (a) without and (b–d) with variant selection. The conditions of prediction in Figure 9a–c are indicated by arrows a–c in Figure 8, respectively. (e,f) ODF sections and pole figures for the optimum prediction by DBOR shown in Figure 9c. (a–c) and (e–h) Predictions based on the observed β texture in Figures 3b and 4d–f and (d) prediction based on the predicted β texture in Figure 6d–h. Contour levels are (a–e) 2, 4, 6... and (f–h) 1, 2, 3...

Variant selection probabilities $\rho(g)$ for the optimal predictions by DBOR and EDBOR $n = 1$ are shown in Figure 10; 12 variants in $\beta \rightarrow \alpha$ -hex reduced to 3 and 7 child orientations for $\{001\}\langle 100\rangle$ and $\{112\}\langle 11\bar{1}\rangle$ because of their symmetries, respectively. Since the multiplicity of the child orientations was not the same for all the child orientations of $\{112\}\langle 11\bar{1}\rangle$, the values of ρ for all of the 12 variants are shown for $\{112\}\langle 11\bar{1}\rangle$ in Figure 10, whereas the multiplicity was the same, 4, for all the child orientations of $\{001\}\langle 100\rangle$. The probabilities of selecting variants $g_{\alpha\text{-hex}1}$ of $\{001\}\langle 100\rangle$ and $g_{\alpha\text{-hex}1}$ and $g_{\alpha\text{-hex}2}$ of $\{112\}\langle 11\bar{1}\rangle$, the orientations of which lie around $\{01\bar{1}3\}\langle 2\bar{1}10\rangle$ and $\{01\bar{1}2\}\langle 2\bar{1}10\rangle$, were relatively large, particularly for $g_{\alpha\text{-hex}1}$ for both parent orientations. EDBOR $n = 1$ predicted larger values of $\bar{\rho}$ than unity for these parent orientations, suggesting selective growth beyond grain boundaries surrounding the parent grains; the total volume of child grains was 1.2 to 1.6 times the volume of the parent grains (see $\bar{\rho}$ in Figure 10b). However, since the values of ρ for the major components in α -hex (e.g., $g_{\alpha\text{-hex}1}$ and 2) were close to each other for DBOR and EDBOR $n = 1$, both predictions resulted in very similar α -hex textures.

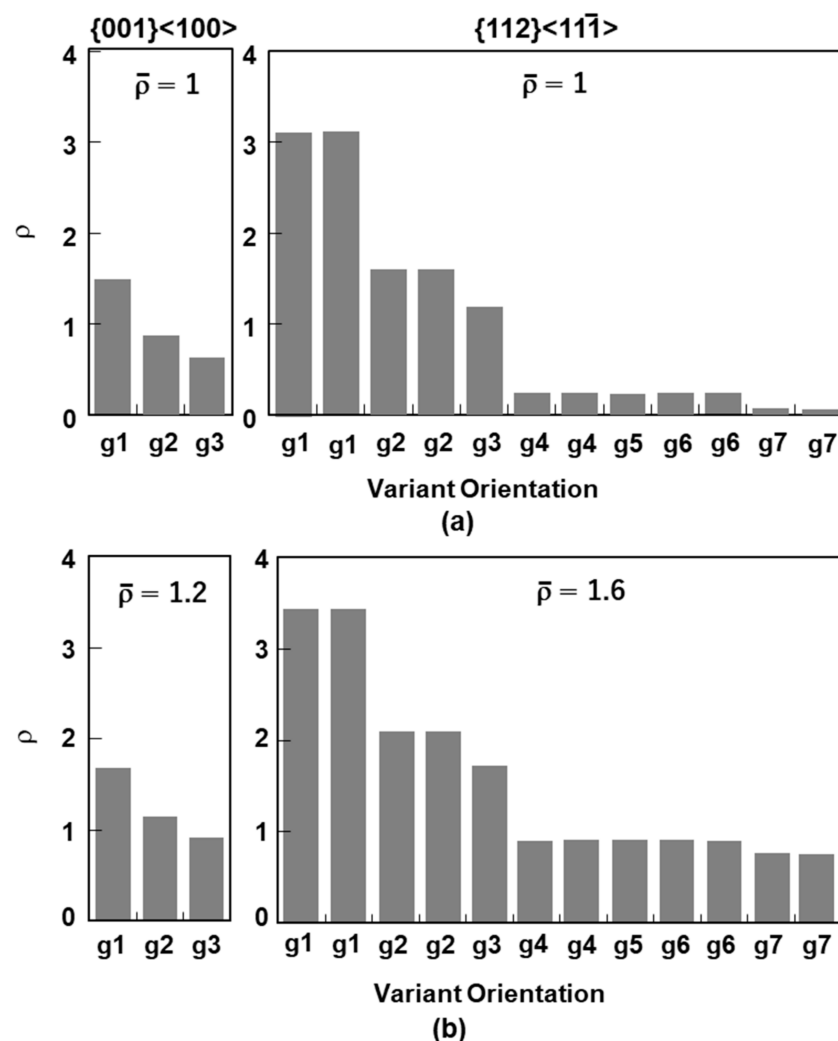


Figure 10. Variant selection probability, ρ , for parent orientations $\{001\}\langle 100\rangle$ and $\{112\}\langle 11\bar{1}\rangle$ in the optimum prediction by (a) DBOR and (b) EDBOR $n = 1$ for $\beta \rightarrow \alpha$ -hex transformation in Figure 9b,c,e-h. The conditions for optimum prediction are indicated by (a) arrow b and (b) arrow c in Figure 8. See Table 2 for variant orientations.

6. Discussion

The DBOR scheme excellently reproduced both of α -hex $\rightarrow \beta$ and $\beta \rightarrow \alpha$ -hex transformation textures in CP-Ti observed in situ by pulsed neutron diffraction. Although the

parameters of DBOR, ω and ζ , were determined by RMS fitting, relatively small numbers of the parameters were required to be adjusted for the reproduction of all the areas of ODFs in the observed textures. For $\beta \rightarrow \alpha$ -hex, simple DBOR even with all the parameters being unity could reproduce the observed texture well, which clearly suggests the applicability of the DBOR scheme to texture memory in hexagonal metals. Here, we discuss how nucleation that satisfies DBOR occurs in phase transformation in hexagonal metals and how these nuclei grow.

6.1. Special Boundary for DBOR

DBOR nucleation occurs on the special boundaries listed in Table 1 as aforementioned. For $\beta \rightarrow \alpha$ -hex transformation, it has been previously observed that grain boundary α -hex nucleates satisfying DBOR, and Widmanstätten α -hex of the same orientation grows on both sides of the special boundaries [45,46], which is closely related to the slip transmission across grain boundaries. It was also reported from EBSD observation that the allowed misorientation from DBOR was less than about 15° , and less misoriented variants tended to be chosen first [46], which supports the DBOR concept of variant selection in this study and our choice of a deviation around 10° from the exact DBOR.

For α -hex $\rightarrow \beta$ transformation, there are five types of special boundaries at which β grains on either side rotate to one another by 10.5 to 90° about the c-axis or the axes near $\langle 2\bar{1}\bar{1}0 \rangle$. For the 10.5° and 60° boundaries, the rotation axes are exactly the c-axis and $\langle 2\bar{1}\bar{1}0 \rangle$, respectively. For the other 60.8 , 63.3 , and 90° boundaries, the rotation axes are inclined from $\langle 2\bar{1}\bar{1}0 \rangle$ by about 5 to 17° . Therefore, they are mostly the rotations about the $\langle 2\bar{1}\bar{1}0 \rangle$ axis. To the best of our knowledge, there seems to be no previous report on the special boundaries in α -hex $\rightarrow \beta$. For $\beta \rightarrow \alpha$ -hex transformation, as reported by Shi et al. [46], there are four types of special boundaries at which β grains on either side rotate to one another by 10.5 to 60° about either $\langle 110 \rangle$ or $\langle 111 \rangle$. One of the four types is of the rotation about $\langle 111 \rangle$ by 60° , i.e., the twin-related $\Sigma 3$ boundary. On all the special boundaries, there is one variant that exactly satisfies DBOR. In addition, when allowing about 10° deviation from the exact DBOR, there is another variant nearly satisfying DBOR, since BOR has three and six pairs of variants that rotate to each other by 10.5° for both α -hex $\rightarrow \beta$ and $\beta \rightarrow \alpha$ -hex, respectively.

6.2. Special Boundary in Texture-Free Structures

Then, the first question to ask is how frequently the potential nucleation sites for DBOR exist in materials and whether this frequency is sufficient to influence the transformation texture. The probability with which the nuclei fulfil DBOR on plane boundaries can be calculated by evaluating how frequently parent grains of orientations around $\Delta g_k^{-1} \cdot \Delta g_i \cdot g$ exist in grain structures as introduced in Equation (9) (see also Figure 1a). Therefore, given the orientations of parent grains g_1 and g_2 on either side of a grain boundary, the deviation from DBOR Δg_{BOR} in α -hex $\rightarrow \beta$ can be evaluated by the rotation

$$\Delta g_{BOR} = \Delta g_k^{-1} \cdot \Delta g_i \cdot g_1 \cdot g_2^{-1} = \Delta g^{-1} \cdot g_k^c \cdot \Delta g \cdot g_i^h \cdot g_1 \cdot g_2^{-1}, \quad (27)$$

which is basically the same expression as that reported in [46].

In grain structures without textures, the probability for a plane boundary to have at least one DBOR variant is about 13 and 19% for α -hex $\rightarrow \beta$ and $\beta \rightarrow \alpha$ -hex transformations, respectively assuming $\Delta g_{BOR} < 10^\circ$; we randomly generated 2×10^4 orientation pairs of the parent grains, g_1 and g_2 , and calculated Δg_{BOR} . If we allow a few degrees more for the deviation, the probabilities increase somewhat. However, they are still small compared to the probability for DKS in steel, which is about 60% calculated in a similar way.

On triple junctions, the probability increases twice for the growth by migration of coherent interfaces such as martensite as shown in Figure 1b, and it increases three times (${}_3C_2$) when the nuclei can grow by coherent as well as incoherent (or semi-coherent) interphase boundaries as shown Figure 1c. However, even for triple junctions, DBOR

nucleation can occur only on about 50% of them, which contrasts with the fact that DKS can occur almost always on triple junctions in steel as observed experimentally [16].

6.3. Influence on Special Boundary by Strong Texture

For strong textures in parent structures, the probability may change greatly. For example, in the α -hex \rightarrow β transformation shown in Figure 3, the TD-split c-axis components inclined from ND by 30 or 45° with $\langle 2\bar{1}\bar{1}0 \rangle$ in RD (nearly $\{01\bar{1}3\}\langle 2\bar{1}\bar{1}0 \rangle$ and $\{01\bar{1}2\}\langle 2\bar{1}\bar{1}0 \rangle$) are composed of two symmetric components inclined in the opposite directions, between which there are the 60 or 90° special boundaries (Type II or V), respectively (see Table 2). The DBOR variants on these special boundaries form the $\{112\}\langle 11\bar{1} \rangle$ and $\{001\}\langle 100 \rangle$ components in β . Furthermore, in the β structure, the $\{112\}\langle 11\bar{1} \rangle$ components are also composed of two symmetry components, between which there are the 60° special boundaries (Type III) in $\beta \rightarrow \alpha$ -hex; the symmetry components are described in more detail in Section 6.7. Moreover, between the $\{112\}\langle 11\bar{1} \rangle$ and $\{001\}\langle 100 \rangle$ components, there are boundaries close to type IV special boundaries (deviated by about 16°). The DBOR variants on these special boundaries form the $\{01\bar{1}3\}\langle 2\bar{1}\bar{1}0 \rangle$ and $\{01\bar{1}2\}\langle 2\bar{1}\bar{1}0 \rangle$ components as well as the other major components observed in the final α -hex structure as listed in Table 2 (bold letters with * or **). Therefore, the presence of strong textures can largely increase the density of the special boundaries, and this is the case for the rolled and annealed CP-Ti sheets observed in this study.

6.4. Influence of Special Boundary in α -hex \rightarrow β on Heating

This influence on special boundaries by textures can be evaluated by defining a probability ratio of these special grain boundaries relative to the texture-free material, TF (texture factor), as

$$TF = \frac{1}{N_k} \cdot \sum_{k=1}^{N_k} f_{\alpha\text{-hex}} \left(\Delta g^{-1} \cdot g_k^c \cdot \Delta g \cdot g \right), \quad (28)$$

for α -hex \rightarrow β transformation as depicted in Figure 1a; for $\beta \rightarrow \alpha$ -hex, TF is defined in a similar way by changing $f_{\alpha\text{-hex}}$ to f_{β} and g_k^c to g_k^h . TF is the ratio of the probability of existence of the special boundaries surrounding the parent grains of the orientation g to that for texture-free materials, and, of course it is included in the formulation of $\rho(g)$ in DBOR and EDBOR (Equations (10) and (16)). Therefore, $\rho(g)$ contains the information for this influence by textures.

For instance, the $\bar{\rho}$ for α -hex \rightarrow β transformation in Figure 7a is 1.7 and 0.77 for $\{01\bar{1}3\}\langle 2\bar{1}\bar{1}0 \rangle$ and $\{\bar{1}2\bar{1}5\}\langle 10\bar{1}0 \rangle$, respectively. From these values and the values of $\omega = 0.6$ and $\delta = 0.39$ for the prediction, TFs are obtained from Equation (16) to be 2.2 and 0.63 for the above parent orientations, respectively, neglecting the influence of ζ . Therefore, the probability of having DBOR variants on the grain boundaries around $\{01\bar{1}3\}\langle 2\bar{1}\bar{1}0 \rangle$ and $\{\bar{1}2\bar{1}5\}\langle 10\bar{1}0 \rangle$ grains are about 29% ($13\% \times 2.2$) and 8.2% ($13\% \times 0.63$) on plain boundaries, respectively, two to three times more on triple junctions and even more for grain corners. Therefore, most of the recrystallized components around $\{01\bar{1}3\}\langle 2\bar{1}\bar{1}0 \rangle$ are surrounded by grain boundaries with potential nucleation sites for DBOR, whereas the $\{\bar{1}2\bar{1}5\}\langle 10\bar{1}0 \rangle$ components are scarcely surrounded by such boundaries. This probability was evaluated and reflected as volume change (the violation of local volume conservation) in the EDBOR prediction so that a better prediction could be attained as explained above.

In [4], it has been suggested that only the growth components around $\{01\bar{1}3\}\langle 2\bar{1}\bar{1}0 \rangle$ should transform with an unknown variant selection in α -hex \rightarrow β . This is exactly the case that the above analysis by EDBOR suggests. As shown in Figure 7, all the variants of the $\{01\bar{1}3\}\langle 2\bar{1}\bar{1}0 \rangle$ parent grains, which transform to $\{001\}\langle 100 \rangle$ and $\{112\}\langle 11\bar{1} \rangle$, are preferentially chosen to nucleate and grow to $\bar{\rho} = 1.5$ –1.7 times of the volume of the $\{01\bar{1}3\}\langle 2\bar{1}\bar{1}0 \rangle$ parent grains, while the variants from the $\{\bar{1}2\bar{1}5\}\langle 10\bar{1}0 \rangle$ grains are less frequently chosen for their total volume to shrink to $\bar{\rho} = 0.77$ times of the volume of the parent grains. Therefore, it is very likely that upon heating to β temperature, the DBOR variants are preferentially selected because of lower interphase boundary energy nucleating

earlier on the special boundaries around the $\{01\bar{1}3\}\langle 2\bar{1}\bar{1}0\rangle$ as well as $\{01\bar{1}2\}\langle 2\bar{1}\bar{1}0\rangle$ grains and preferentially growing into not only the parent grains but also other grains such as the $\{\bar{1}2\bar{1}5\}\langle 10\bar{1}0\rangle$ grains. This growth process is consistent with the metallographical analysis of CP-Ti in that, whereas the grain size of α -hex before transformation is only about 20 μm , that of β is very large at around 1 mm [4].

6.5. Influence of Special Boundary in $\beta \rightarrow \alpha$ -hex on Cooling

For $\beta \rightarrow \alpha$ -hex transformation, the $\bar{\rho}$ for the prediction by EDBOR $n = 1$ in Figure 10b is 1.2 and 1.6 for $\{100\}\langle 001\rangle$ and $\{112\}\langle 11\bar{1}\rangle$, respectively. From these values and the values of $\omega = 0.7$ and $\delta = 0.17$ for the prediction, TFs are obtained as 1.5 and 2.0 for the above orientations, respectively, neglecting the influence of ζ . Therefore, the probability of having DBOR variants on the grain boundaries in the observed β is about 40 ($\sim 19 \times 2$) and close to 100% on plain boundaries and triple junctions, respectively, large enough values to apply the DBOR mechanism to the texture prediction.

Since both $\{001\}\langle 100\rangle$ and $\{112\}\langle 11\bar{1}\rangle$ parent grains are surrounded by many boundaries with potential nucleation sites for DBOR as explained above, and the parent grain size is as large as 1 mm, an extensive growth of the child phase into multiple parent grains (by migration of incoherent interfaces) would not occur as in the α -hex $\rightarrow \beta$ transformation. Therefore, EDBOR does not predict more accurately than the simple DBOR as seen in Figures 8 and 9, which is in good agreement with the observation that migrating interfaces of $\beta \rightarrow \alpha$ -hex transformation are coherent ones like martensite transformation [29,45]. Since the value of ω for the optimum DBOR prediction is from 0.7 to 0.8 and close to unity, the nucleation and growth should be dominated by DBOR variants as expected.

6.6. Coexistence of Differently Oriented Laths in $\beta \rightarrow \alpha$ -hex

It is worth noting that when one variant exactly satisfies DBOR on a grain boundary, there is one more variant that nearly satisfies DBOR with the deviation of 10.5° , since 6 and 12 variants in BOR of $\beta \rightarrow \alpha$ -hex and $\beta \rightarrow \alpha$ -hex transformations are 3 and 6 pairs of closely orientated variants of 10.5° rotation about $\langle 110\rangle$ and the c-axis, respectively. Therefore, the 10.5° rotated variant can coexist with the exact DBOR variant as reported in [29], which have different lath orientations. An example is $g_{\alpha 1} \{01\bar{1}3\}\langle 2\bar{1}\bar{1}0\rangle$ ($\varphi_1 = 0^\circ$, $\Phi = 30^\circ$, and $\varphi_2 = 30^\circ$) and $g_{\alpha 2}$ ($\varphi_1 = 0^\circ$, $\Phi = 30^\circ$, and $\varphi_2 = 19.5^\circ$) nucleating on the type III boundary between the sample-symmetry pair of $\{112\}\langle 11\bar{1}\rangle$ (see Figure 11), which are rotated by 10.5° about the c-axis to each other (see Table 2). Moreover, more disoriented variants can also coexist. On the same type III boundary, the $g_{\alpha 1} \{01\bar{1}3\}\langle 2\bar{1}\bar{1}0\rangle$ and $g_{\alpha 3} \{01\bar{1}0\}\langle 2\bar{1}\bar{1}0\rangle$, which are rotated by 60° about $\langle 2\bar{1}\bar{1}0\rangle$ to each other, satisfy DBOR and can nucleate at the same place. Therefore, these DBOR variants can nucleate and grow either on the opposite sides of the grain boundary or on the same side to coexist as differently oriented laths as previously reported [19,45].

6.7. Common $\{110\}$ Plane Variants in $\beta \rightarrow \alpha$ -hex

Another point to be mentioned is nearly common parallel $\{110\}$ planes of adjacent β grains, which have been repeatedly reported as the planes to which the basal plane of α -hex tend to be parallel [19,23,29,30,45,46]. In the observed texture of β , the sample-symmetry pair of $\{112\}\langle 11\bar{1}\rangle$ has three common $\{110\}$ planes, of which plane normals ($\langle 110\rangle$) are in the directions inclined by 30 and 90° from ND to TD, shown as gray triangles in Figure 11a. These symmetry pair share the $\langle 111\rangle$ direction in RD as shown in Figure 11b. Then, the DBOR variants $g_{\alpha\text{-hex}1}$ and $g_{\alpha\text{-hex}3}$ fulfil the common $\{110\}$ plane rule on these $\{110\}$ planes. In the directions shown by arrow a in Figure 11, the $\{001\}\langle 100\rangle$ and $\{112\}\langle 11\bar{1}\rangle$ components nearly also share $\{110\}$ planes. Then, there are near-DBOR variants, $g_{\alpha\text{-hex}1}$, of the $\{001\}\langle 100\rangle$ component and $g_{\alpha\text{-hex}1}$ and $g_{\alpha\text{-hex}2}$ of the $\{112\}\langle 11\bar{1}\rangle$ components (see Table 2), which satisfy the common $\{110\}$ plane rule. However, although there are another pair of nearly parallel $\{110\}$ planes in the directions rotated by about 50° from ND to RD (arrow b in Figure 11) for $\{001\}\langle 100\rangle$ and $\{112\}\langle 11\bar{1}\rangle$ components, which deviate by

about 10° from each other, no DBOR variant exists sharing these nearly common $\{110\}$ planes. This is because the $\langle 111 \rangle$ directions perpendicular to the common $\{110\}$ of the two components, which should be parallel to $\langle 2\bar{1}10 \rangle$ in BOR, deviate by about 21 or 90° (not multiples of 60°) from each other as shown in Figure 11b. Hence, the common $\{110\}$ plane rule does not apply to this case, and this should be the reason why the intensities of the $\langle 0001 \rangle_\alpha$ poles in these directions (about 50° from ND to RD) are not strong in the final α -hex textures as shown in Figures 4g and 9f, whereas the $\{110\}$ poles in the directions are relatively strong in the observed β texture. Therefore, the common $\{110\}$ plane rule is not sufficient to determine the variant selection, since the common $\{110\}$ plane rule is a part of the DBOR rules that should determine the variants.

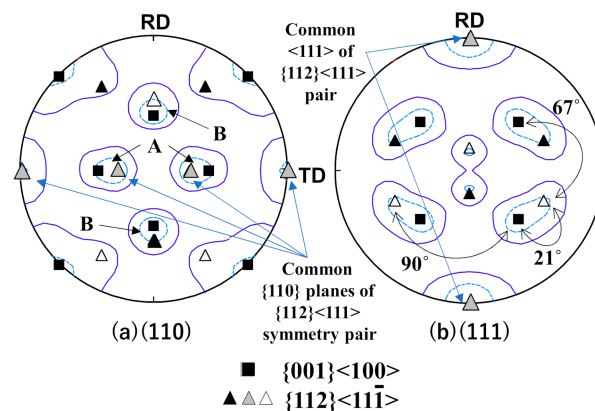


Figure 11. Orientations of (a) (110) and (b) (111) poles of $\{001\}\langle 100 \rangle$ and $\{112\}\langle 11\bar{1} \rangle$ components in β structure. Two components in a $\{112\}\langle 11\bar{1} \rangle$ sample–symmetry pair are distinguished by black and white triangles. Gray triangles represent common poles of the symmetry pair.

6.8. Influence of ζ , Nucleation Rates, and Macro Zones

Of interest are nucleation rates on the special boundaries. The frequency of nucleation is in general different in different types of nucleation site because of the different densities and chemical energy of the site (e.g., grain boundary energy), shape of embryos, and so on. The classical theory of nucleation describes the total nucleation rate as the sum of nucleation rates at different potential nucleation sites as given by [47,48]

$$\dot{N} = \sum_j Z_j \cdot \frac{k \cdot T}{h} \cdot \exp\left(-\frac{\Delta G_j^* + Q_j}{k \cdot T}\right) \quad (29)$$

where j denotes the type of nucleation site, and Z_j , k , and h are the number density of the potential nucleation site, Boltzmann constant, and Planck's constant, respectively. ΔG_j^* is the change in Gibbs free energy dependent on internal energy change by the phase transformation, grain boundary energy that is gained by removing it, interphase interfacial energy, and shape of embryos. Q_j is the activation energy of jumping atoms across interphase boundaries. The $\rho(g)$ approximates the nucleation rates in Equation (29) as a function of variant orientation. The decrease in the interfacial energy by having coherent or semi-coherent interfaces by DBOR decreases ΔG_j^* and increases the nucleation rate, as approximated by Equations (10), (16) and (17).

The $\rho(g)$ mainly calculates the influence of parent textures on Z_j in Equation (29), while the weight factor of ζ accounts for other influence than the parent texture such as those due to uneven spatial distribution of texture components such as macro-zones [19] and grain boundary energy in ΔG_j^* . For the macro-zone in α -hex, it was observed (by 3D-EBSD) in CP-Ti, which had a similar texture to the observed texture in this study, that the densities of small-angle grain boundary and the boundary around 90° rotation about $\langle 2\bar{1}10 \rangle$ (type V) were substantially larger than those of the random distribution (by about two and seven times, respectively) [18]. This observation is roughly consistent with the above discussion.

However, the number density of boundary around 60° about $\langle 2\bar{1}\bar{1}0 \rangle$ (type II and close to types III and IV) was surprisingly lower than the random distribution (from 0.6 to 0.9 times), which should be much larger than unity based on the above analysis.

The number density of boundaries, for which the rotation between crystals on both sides is ΔR , can be evaluated from textures as a ratio of that in the random boundaries,

$$GBD(\cdot R) = \frac{1}{N_i} \cdot \sum_{i=1}^{N_i} \oint f(\Delta R \cdot \Delta g_i^h \cdot g) \cdot f(g) dg. \quad (30)$$

Since $f(\Delta R \cdot \Delta g_i^h \cdot g) \cong f(g)$ for small-angle boundaries ($\Delta R \rightarrow 0$), it is true that

$$GBD(\text{small angle}) = \oint f(g)^2 dg. \quad (31)$$

The value of Equation (31) for the observed α -hex texture in Figures 3a and 4a–c is about 3.5, which is only a half of the reported number density of small-angle boundaries, although the texture observed in this study was a little stronger than that of the material used in [18]. This indicates the presence of the macro-zone in which similarly oriented grains cluster together; texture analysis assumes random spatial distribution of texture components. Another point is that the reported number density of the boundary around 60° about $\langle 2\bar{1}\bar{1}0 \rangle$, which should be larger than the random density (see Table 2), was smaller than the random density as explained above. Thus, considering the high density of small-angle boundaries together, it is very likely that the grains with the major orientation $\{01\bar{1}3\}\langle 2\bar{1}\bar{1}0 \rangle$ particularly congregate into a macro-zone so that the density of special boundaries of type II and near-types III and IV (between the sample–symmetry pair of $\{01\bar{1}3\}\langle 2\bar{1}\bar{1}0 \rangle$) decreases, whereas that of small-angle boundaries increases as reported in [18]. Therefore, the values of ζ in the optimum prediction are large only for the type V boundaries ($\zeta = 3$) (see Table 2), which is in good agreement with the reported ratio of number densities between near-type II and type V boundaries (about 2.7) [18]. The value of ζ for the small-angle boundaries can be large due to its higher number density in contrast to that expected from the texture. However, its small grain boundary energy [49,50] can cancel out the effect.

For $\beta \rightarrow \alpha$ -hex transformation, since the energy of the small-angle boundary in bcc metal is also relatively small as compared to high-angle boundaries [50], ζ for the type I special boundary may be as small as predicted ($\zeta \rightarrow 0$), although the nucleation of α -hex on the type I special boundary has been observed experimentally [29]. The value of ζ for the type II special boundary was determined to be three times larger than that for the other high-angle special boundaries. This indicates that the energy of the type II boundary can be larger than that of the type III ($\Sigma 3$) and the type IV (60° about $\langle 110 \rangle$) boundaries, in which low energy boundaries have been reported to exist [50]. However, the grain boundary energy is not only dependent on relative orientation between adjacent grains but also boundary plane inclination. More research would be required on the grain boundary characterization of high-temperature β to discuss this result further.

6.9. Simulation of Further Heating Cycles

Whether the strength of textures decreases or increases after several consecutive heating cycles over the β transus is a question that one would like to ask to control the anisotropy of properties in products of hexagonal metals. Thus, the texture evolution during such heat treatment has been simulated using the optimum conditions described above; EDBOR $n = 2$ ($\omega = 0.18$) and DBOR ($\omega = 0.8$) for α -hex $\rightarrow \beta$ and $\beta \rightarrow \alpha$ -hex with ζ listed in Table 2, respectively.

Two simulations are shown in Figures 12 and 13. One is a continuation of the heating cycle in the present experiment, and the observed α texture shown in Figures 3c and 4g–i was used as the starting texture of the second cycle. As seen in Figure 12, the textures of β as well as α -hex phases greatly developed and were strengthened by the second heating

cycle; the final α -hex texture was calculated using the computed β texture. Although the textures consisted of texture components similar to the observed textures, the intensity maxima in the pole figures of β and α -hex phases during and after the second heating cycle were as large as about 16 and 100 times the random intensity, respectively.

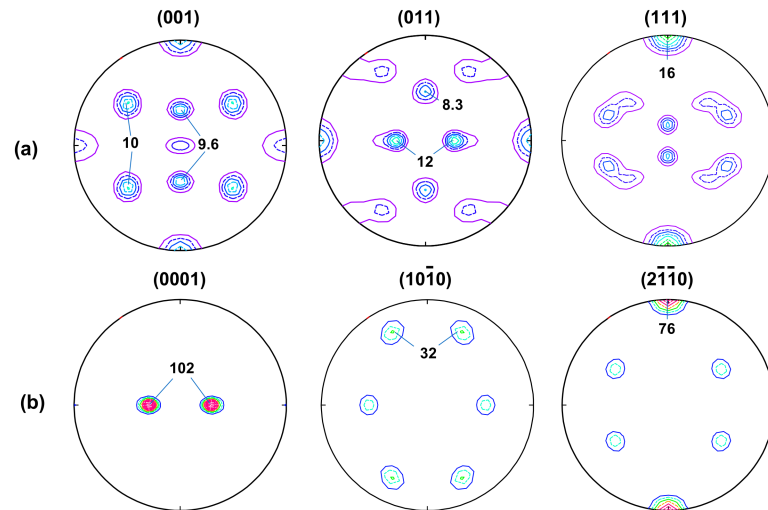


Figure 12. Pole figures of predicted (a) β and (b) α -hex textures in the second heating cycle based on the observed texture shown in Figures 3c and 4g–i.

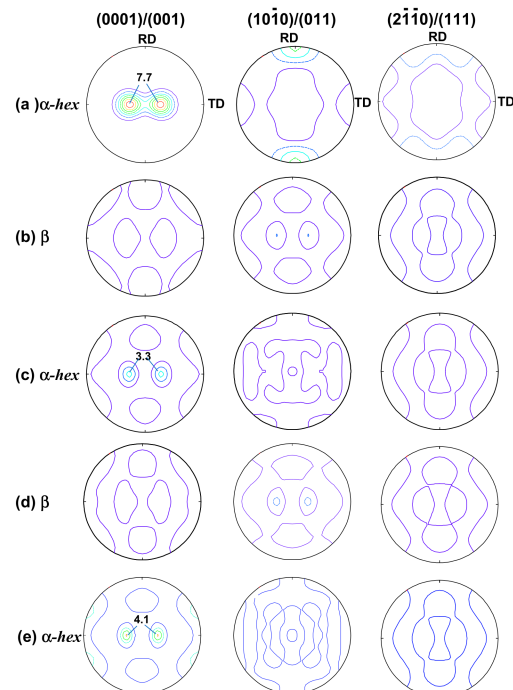


Figure 13. Pole figures of model (a) α -hex \rightarrow (b) β \rightarrow (c) α -hex \rightarrow (d) β \rightarrow (e) α -hex heating cycles. Contour levels are 1,2,3...

The other was two consecutive heating cycles of a model texture of a recrystallized Zr sheet. The model texture was based on an in situ observation of textures of α -hex Zr at 750 °C by Wenk et al. [5]. The reported model α -hex structure composed of a mixture of three Gaussian components of orientations $(0^\circ, 30^\circ, 0^\circ)$, $(0^\circ, 30^\circ, 30^\circ)$, and $(0^\circ, 0^\circ, 0^\circ)$ in Euler angles, the volume ratio of which was 60%:30%:10% [5], respectively, was used as the starting α -hex texture. A Gaussian distribution of 20° half-width was used for each component [34]. Although this texture was similar to the observed texture for CP-Ti

in Figures 3a and 4a–c, the texture was somewhat weaker, and it had a relatively fewer components with $\langle 2\bar{1}10 \rangle$ in RD. Transformation calculations were then applied as explained above. In contrast to the case of CP-Ti, the texture of α -hex was slightly weakened after the first heating cycle, and then a similar but slightly strengthened α -hex texture appeared after the second heating cycle, as shown in Figure 13. It is also noteworthy that these simulated texture changes well resemble those observed experimentally [5]. Therefore, the texture memory phenomenon in hexagonal metals is largely dependent on the strength and type of the initial textures, and there should be a critical intensity or severity of initial textures above which the texture significantly develops by repeating heating cycles to above the β transus.

7. Conclusions

Texture memory and its formation mechanisms in hexagonal metals have been investigated via a prediction method with variant selection mechanisms and in situ observation of textures by pulsed neutron diffraction. The conclusions are as follows.

- (1) Mathematical methods for the prediction of transformation textures in hexagonal metals using harmonic expansion have been described, and a variant selection mechanism has also been formulated in which nucleation and growth preferentially occur when variants satisfy BOR with two adjoining parent grains at the same time (DBOR) for both α -hex \rightarrow β and $\beta \rightarrow$ α -hex transformations. Different nucleation and growth rates for different potential nucleation sites for DBOR, which are five and four types of special grain boundaries in α -hex \rightarrow β and $\beta \rightarrow$ α -hex transformations, respectively, are included in the formulation.
- (2) The variant selection by DBOR has been extended to describe the selected DBOR variants to grow not only into one parent grain (the local material conservation) but also into multiple parent grains with non-linear probabilities (EDBOR).
- (3) The special boundaries where DBOR is satisfied in α -hex \rightarrow β transformation are of 10.5° rotation about the c-axis and 60° , 60.8° , 63.3° , and 90° rotations about $\langle 2\bar{1}10 \rangle$ or axes near to it. Those in $\beta \rightarrow$ α -hex transformation are of 10.5° , 49° , 60° rotations about $\langle 110 \rangle$ and 60° rotation about $\langle 111 \rangle$ ($\Sigma 3$). In texture-free materials, the probability of the existence of these special boundaries is as small as about 13 and 19% in α -hex \rightarrow β and $\beta \rightarrow$ α -hex, respectively. However, textures of parent phases can increase this probability, and this is the case for the α -hex \rightarrow $\beta \rightarrow$ α -hex transformation in CP-Ti rolled sheets.
- (4) The analysis of in situ observed bulk textures of CP-Ti rolled sheets by pulsed neutron diffraction revealed that the texture memory in CP-Ti can be thoroughly explained by the DBOR mechanism. The transformation texture formation in α -hex \rightarrow β obeys to EDBOR $n = 2$ (squared probability) in which the nucleation and growth rate for the special boundary of 90° rotation about $\langle 2\bar{1}10 \rangle$ is three times larger than that for the other special boundaries, while the transformation in $\beta \rightarrow$ α -hex obeys DBOR well with the local material conservation. The higher rate for the special boundary of 90° rotation is ascribed to a higher number density of this special boundary in CP-Ti, which relates to the macro-zone formation.
- (5) For $\beta \rightarrow$ α -hex transformation, the nucleation and growth rates for the special boundaries with rotations of 10.5° and 49° about $\langle 110 \rangle$ are predicted to be as small as zero and three times larger than those for the other high-angle special boundaries, which can be ascribed to lower and higher grain boundary energies for these special boundaries than the others, respectively. However, even with all the parameters of ω and ζ being unity (or ideal), DBOR could predict the texture change in $\beta \rightarrow$ α -hex transformation well.
- (6) By considering the DBOR mechanism, several well-known phenomena in CP-Ti, such as the preferential transformation of the growth components around $\{01\bar{1}3\}\langle 2\bar{1}10 \rangle$ in α -hex \rightarrow β , the coexistence of differently oriented laths, and the common $\{110\}$ plane variants in $\beta \rightarrow$ α -hex, can be well understood.

- (7) The model calculations of repeating the α -hex \rightarrow β \rightarrow α -hex heating cycles suggest that there should be a critical strength of the texture above which the texture develops significantly by repeating the heating cycles.

Author Contributions: Conceptualization, T.T.; methodology, T.T.; investigation, T.T. and Y.O.; data curation, S.C.V.; funding acquisition, S.S. All authors have read and agreed to the published version of the manuscript.

Funding: This research received no external funding.

Institutional Review Board Statement: Not applicable.

Informed Consent Statement: Not applicable.

Acknowledgments: We gratefully acknowledge H.-R. Wenk's kind permission on behalf of the authors of Lonardelli et al. The work has benefitted from the use of the Los Alamos Neutron Science Center (LANSCE) at Los Alamos National Laboratory. Los Alamos National Laboratory is operated by Triad National Security, LLC, for the National Nuclear Security Administration of the U.S. Department of Energy under contract number 89233218NCA000001.

Conflicts of Interest: The authors declare no conflict of interest.

References

- Ray, R.K.; Jonas, J.J. Transformation textures in steels. *Int. Mater. Rev.* **1990**, *35*, 1–36. [\[CrossRef\]](#)
- Hutchinson, B.; Kestens, L. Origins of texture memory in steels. *Ceram. Trans.* **2009**, *201*, 281–290.
- Tomida, T.; Wakita, M.; Yasuyama, M.; Sugaya, S.; Tomota, Y.; Vogel, S.C. Memory effects of transformation textures in steel and its prediction by the double Kurdjumov–Sachs relation. *Acta Mater.* **2013**, *61*, 2828–2839. [\[CrossRef\]](#)
- Lonardelli, I.; Gey, N.; Wenk, H.-R.; Humbert, M.; Vogel, S.C.; Lutterotti, L. In situ observation of texture evolution during $\alpha \rightarrow \beta$ and $\beta \rightarrow \alpha$ phase transformations in titanium alloys investigated by neutron diffraction. *Acta Mater.* **2007**, *55*, 5718–5727. [\[CrossRef\]](#)
- Wenk, H.-R.; Lonardelli, I.; Williams, D. Texture changes in the hcp-bcc-hcp transformation of zirconium studied in situ by neutron diffraction. *Acta Mater.* **2004**, *52*, 1899–1907. [\[CrossRef\]](#)
- Humbert, M.; Gey, N. Elasticity-based model of the variant selection observed in the β to α phase transformation of a Zircalloy-4 sample. *Acta Mater.* **2003**, *51*, 4783–4790. [\[CrossRef\]](#)
- Daymond, M.R.; Holt, R.A.; Cai, S.; Mosbrucker, P.; Vogel, S.C. Texture inheritance and variant selection through an hcp-bcc-hcp phase transformation. *Acta Mater.* **2010**, *58*, 4053–4066. [\[CrossRef\]](#)
- Kimmins, S.T.; Gooch, D.J. Austenite memory effect in 1 Cr–1 Mo–0.75V (Ti, B) steel. *Met. Sci.* **1983**, *17*, 519–532. [\[CrossRef\]](#)
- Nakada, N.; Tsuchiyama, T.; Takaki, S.; Hashizume, S. Variant selection of reversed austenite in lath martensite. *ISIJ Int.* **2007**, *47*, 1527–1532. [\[CrossRef\]](#)
- Li, X.; Li, K.; Cai, Z.; Pan, J. Review of austenite memory effect in HAZ of B containing 9% Cr martensitic heat resistant steel. *Metals* **2019**, *9*, 1233. [\[CrossRef\]](#)
- Kurdjumov, G.; Sachs, G. Über den mechanismus der stahlhärtung. *Z. Phys.* **1930**, *64*, 325–343. [\[CrossRef\]](#)
- Burgers, W.G. On the process of transition of the cubic-body-centered modification into the hexagonal-close-packed modification of zirconium. *Physica* **1934**, *1*, 561–586. [\[CrossRef\]](#)
- Vakhitova, E.; Sornin, D.; Wright, J.; Tomida, T.; Francois, M.J. In situ synchrotron analysis of phase transformation at high temperatures in ODS ferritic steel. *Mater. Sci.* **2020**, *55*, 5600–5612. [\[CrossRef\]](#)
- Lischewski, I.; Gottstein, G. Nucleation and variant selection during the α - γ - α phase transformation in microalloyed steel. *Acta Mater.* **2011**, *59*, 1530–1541. [\[CrossRef\]](#)
- Hata, K.; Wakita, M.; Fujiwara, K.; Kawano, K.; Tomida, T.; Sugiyama, M.; Fukuda, T.; Kakeshita, T. In situ EBSD analysis on the crystal orientation relationship between ferrite and austenite during reverse transformation of an Fe-Mn-C alloy. *Mater. Trans.* **2016**, *57*, 1514–1519. [\[CrossRef\]](#)
- Hata, K.; Fujiwara, K.; Kawano, K.; Sugiyama, M.; Fukuda, T.; Kakeshita, T. Reconstruction of the three-dimensional ferrite-austenite microstructure and crystallographic analysis in the early stage of reverse phase transformation in an Fe-Mn-C alloy. *ISIJ Int.* **2018**, *58*, 323–333. [\[CrossRef\]](#)
- Hata, K.; Fujiwara, K.; Kawano, K.; Sugiyama, M.; Fukuda, T.; Kakeshita, T. Three-dimensional EBSD analysis and TEM observation for interface microstructure during reverse phase transformation in low carbon steels. *ISIJ Int.* **2018**, *58*, 742–750. [\[CrossRef\]](#)
- Kelly, M.N.; Glowinski, K.; Nuhfer, N.T.; Rohrer, G.S. The five parameter grain boundary character distribution of α -Ti determined from three-dimensional orientation data. *Acta Mater.* **2016**, *111*, 22–30. [\[CrossRef\]](#)
- Banerjee, D.; Williams, J.C. Perspectives on titanium science and technology. *Acta Mater.* **2013**, *61*, 844–879. [\[CrossRef\]](#)

20. Niinomi, M. Recent research and development in titanium alloys for biomedical applications and healthcare goods. *Sci. Technol. Adv. Mater.* **2003**, *4*, 445–453. [[CrossRef](#)]
21. Griffiths, M.; Winegar, J.E.; Buyers, A. The transformation behaviour of the β -phase in Zr-2.5 Nb pressure tubes. *J. Nucl. Mater.* **2008**, *383*, 28–33. [[CrossRef](#)]
22. Singh, A.K.; Schwarzer, R.A. Texture and anisotropy of mechanical properties in titanium and its alloys. *Z. Metallkd* **2000**, *91*, 702–716.
23. Shih, D.S.; Lin, F.; Starke, E.A., Jr. *Titanium Science and Technology*; Lütjering, G., Zwicker, U., Bunk, W., Eds.; DGM Verlagsges: Oberursel, Germany, 1984; pp. 2099–2106.
24. Peters, M.; Gysler, A.; Lütjering, G. Influence of texture on fatigue properties of Ti-6Al-4V. *Metall. Mater. Trans.* **1984**, *15*, 1597–1605. [[CrossRef](#)]
25. Martin, É.; Azzi, M.; Salishchev, G.A.; Szpunar, J. Influence of microstructure and texture on the corrosion and tribocorrosion behavior of Ti-6Al-4V. *Tribol. Int.* **2010**, *43*, 918–924. [[CrossRef](#)]
26. Lee, T.; Mathew, E.; Rajaraman, S.; Manivasagam, G.; Singh, A.K.; Lee, C.S. Tribological and corrosion behaviors of warm- and hot-rolled Ti-13Nb-13Zr alloys in simulated body fluid conditions. *Int. J. Nanomed.* **2015**, *10*, 207–212.
27. Furuhashi, T.; Takagi, S.; Watanabe, H.; Maki, T. Crystallography of grain boundary precipitates in a β titanium alloy. *MMTA* **1996**, *27*, 1635–1646. [[CrossRef](#)]
28. Stanford, N.; Bate, P.S. Crystallographic variant selection in Ti-6Al-4V. *Acta Mater.* **2004**, *52*, 5215–5224. [[CrossRef](#)]
29. Bhattacharyya, D.; Viswanathan, G.B.; Denkenberger, R.; Furrer, D.; Fraser, H.L. The role of crystallographic and geometrical relationships between alpha and beta phases in an alpha/beta titanium alloy. *Acta Mater.* **2003**, *51*, 4679–4691. [[CrossRef](#)]
30. Shi, R.; Dixit, V.; Viswanathan, G.B.; Fraser, H.L.; Wang, Y. Experimental assessment of variant selection rules for grain boundary α in titanium alloys. *Acta Mater.* **2016**, *102*, 197–211. [[CrossRef](#)]
31. Wenk, H.-R.; Lutterotti, L.; Vogel, S. Texture analysis with the new HIPPO TOF diffractometer. *Nucl. Instrum. Methods Phys. Res. A* **2003**, *515*, 575–588. [[CrossRef](#)]
32. Vogel, S.C.; Lutterotti, L.; Von Dreele, R.B.; Wenk, H.-R.; Williams, D.J. Texture measurements using the new neutron diffractometer HIPPO and their analysis using the Rietveld method. *Powder Diffr.* **2004**, *19*, 65–68. [[CrossRef](#)]
33. Bunge, H.J.; Humbert, M.; Welch, P.I. Texture transformation. *Textures Microstruct.* **1984**, *6*, 81–96. [[CrossRef](#)]
34. Bunge, H.J. *Quantitative Texture Analysis*; Bunge, H.J., Esling, C., Eds.; Deutsche Gesellschaft für Metallkunde: Oberursel, Germany, 1982.
35. Tomida, T.; Wakita, M.; Yoshida, M.; Imai, N. Quantitative prediction of transformation texture in hot-rolled steel sheets by multiple KS relation. *Ceram. Trans.* **2008**, *200*, 325–332.
36. Tomida, T.; Vakhitova, E.; Sornin, D.; Wright, J.; François, M.; Onuki, Y.; Hirano, T.; Hoshikawa, A.; Ishigaki, T.; Sato, S. Texture memory in Si-Mn and ODS steels observed in situ by pulsed neutron and synchrotron X-ray diffractions and prediction by double Kurdjumov-Sachs relation: A concept for intense variant selection. *Metall. Mater. Trans. A* **2021**, *52*, 1368–1381. [[CrossRef](#)]
37. Tanaka, Y.; Tomida, T.; Mohles, V. Quantitative prediction of deformed austenite and transformed ferrite texture in hot-rolled steel sheet. *Mater. Sci. Eng.* **2015**, *82*, 012057. [[CrossRef](#)]
38. Tomida, T.; Wakita, M.; Vogel, S.; Sandim, H.R.Z. Quantitative prediction of transformation texture in steel by double Kurdjumov-Sachs relation. *Mater. Sci. Eng.* **2015**, *82*, 12060.
39. Sharma, H.; Sietsma, J.; Offerman, S.E. Preferential nucleation during polymorphic transformations. *Sci. Rep.* **2016**, *6*, 30860. [[CrossRef](#)]
40. Yoshinaga, N.; Inoue, H.; Kawasaki, K.; Kestens, L.; Cooman, B.C.D. Factors affecting texture memory appearing through a \rightarrow g \rightarrow a transformation in IF steels. *Mater. Trans.* **2007**, *48*, 2036–2042. [[CrossRef](#)]
41. Rietveld, H.M. A profile refinement method for nuclear and magnetic structures. *J. Appl. Cryst.* **1969**, *2*, 65–71. [[CrossRef](#)]
42. Lutterotti, L.; Matthies, S.; Wenk, H.-R.; Schultz, A.S.; Richardson, J.W., Jr. Combined texture and structure analysis of deformed limestone from time-of-flight neutron diffraction spectra. *J. Appl. Phys.* **1987**, *81*, 594–600. [[CrossRef](#)]
43. Matthies, S.; Pehl, J.; Wenk, H.-R.; Lutterotti, L.; Vogel, S.C. Quantitative texture analysis with the HIPPO neutron TOF diffractometer. *J. Appl. Cryst.* **2005**, *38*, 462–475. [[CrossRef](#)]
44. Inoue, H.; Inakazu, N. Determination of orientation distribution functions from incomplete pole figures by iterative series expansion method. *J. Jpn. Inst. Met.* **1994**, *58*, 892–898. [[CrossRef](#)]
45. Bhattacharyya, D.; Viswanathan, G.B.; Fraser, H.L. Crystallographic and morphological relationships between β phase and the Widmanstätten and allotriomorphic α phase at special β grain boundaries in an α/β titanium alloy. *Acta Mater.* **2007**, *55*, 6765–6778. [[CrossRef](#)]
46. Shi, R.; Dixit, V.; Fraser, H.L.; Wang, Y. Variant selection of grain boundary α by special prior β grain boundaries in titanium alloys. *Acta Mater.* **2014**, *75*, 156–166. [[CrossRef](#)]
47. Christian, J. *The Theory of Transformations in Metals and Alloys*; Pergamon Press: Oxford, UK, 1981.
48. Aaronson, H.I.; Enomoto, M.; Lee, J.K. *Mechanisms of Diffusional Phase Transformations in Metals and Alloys*; CRC Press: Boca Raton, FL, USA, 2010.

-
49. Wang, J.; Beyerlein, I.J. Atomic structures of symmetric tilt grain boundaries in hexagonal close packed (hcp) crystals. *Modell. Simul. Mater. Sci. Eng.* **2012**, *20*, 024002. [[CrossRef](#)]
 50. Ratanaphan, S.; Olmsted, D.L.; Bulatov, V.V.; Holm, E.A.; Rolletta, A.D.; Rohrera, G.S. Grain boundary energies in body-centered cubic metals. *Acta Mater.* **2015**, *88*, 346–354. [[CrossRef](#)]